# LJMU Research Online

Simon, P, Semboloni, E, van Waerbeke, L, Hoekstra, H, Erben, T, Fu, L, Harnois-Déraps, J, Heymans, C, Hildebrandt, H, Kilbinger, M, Kitching, TD, Miller, L and Schrabback, T

 CFHTLenS: a Gaussian likelihood is a sufficient approximation for a cosmological analysis of third-order cosmic shear statistics

http://researchonline.ljmu.ac.uk/id/eprint/13370/

Article

# CFHTLenS: a Gaussian likelihood is a sufficient approximation for a cosmological analysis of third-order cosmic shear statistics

P. Simon,[1]* E. Semboloni,[2,3] L. van Waerbeke,[2] H. Hoekstra,[3] T. Erben,[1] L. Fu,[4]
J. Harnois-Déraps,[2,5] C. Heymans,[6] H. Hildebrandt,[1] M. Kilbinger,[7,8]
T. D. Kitching,[9] L. Miller[10] and T. Schrabback[1]

[1]*Argelander Institut für Astronomie, Auf dem Hügel 71, D-53121 Bonn, Germany*
[2]*Department of Physics and Astronomy, University of British Columbia, 6224 Agricultural Road, Vancouver, BC V6T 1Z1, Canada*
[3]*Leiden Observatory, Leiden University, NL-2333 CA Leiden, the Netherlands*
[4]*Shanghai Key Lab for Astrophysics, Shanghai Normal University, 100 Guilin Road, 200234 Shanghai, China*
[5]*Canadian Institute for Theoretical Astrophysics, University of Toronto, ON M5S 3H8, Canada*
[6]*Scottish Universities Physics Alliance, Institute for Astronomy, University of Edinburgh, Royal Observatory, Blackford Hill, Edinburgh EH9 3HJ, UK*
[7]*Institut d'Astrophysique de Paris, UMR7095 CNRS, Université Pierre and Marie Curie, 98 bis boulevard Arago, F-75014 Paris, France*
[8]*CEA/Irfu/SAp Saclay, Laboratoire AIM, F-91191 Gif-sur-Yvette, France*
[9]*Mullard Space Science Laboratory, University College London, Holmbury St Mary, Dorking, Surrey RH5 6NT, UK*
[10]*Department of Physics, Oxford University, Keble Road, Oxford OX1 3RH, UK*

## ABSTRACT

We study the correlations of the shear signal between triplets of sources in the Canada–France–Hawaii Telescope Lensing Survey (CFHTLenS) to probe cosmological parameters via the matter bispectrum. In contrast to previous studies, we adopt a non-Gaussian model of the data likelihood which is supported by our simulations of the survey. We find that for state-of-the-art surveys, similar to CFHTLenS, a Gaussian likelihood analysis is a reasonable approximation, albeit small differences in the parameter constraints are already visible. For future surveys we expect that a Gaussian model becomes inaccurate. Our algorithm for a refined non-Gaussian analysis and data compression is then of great utility especially because it is not much more elaborate if simulated data are available. Applying this algorithm to the third-order correlations of shear alone in a blind analysis, we find a good agreement with the standard cosmological model: $\Sigma_8 = \sigma_8(\Omega_{\rm m}/0.27)^{0.64} = 0.79^{+0.08}_{-0.11}$ for a flat $\Lambda$ cold dark matter cosmology with $h = 0.7 \pm 0.04$ (68 per cent credible interval). Nevertheless our models provide only moderately good fits as indicated by $\chi^2/{\rm dof} = 2.9$, including a 20 per cent rms uncertainty in the predicted signal amplitude. The models cannot explain a signal drop on scales around 15 arcmin, which may be caused by systematics. It is unclear whether the discrepancy can be fully explained by residual point spread function systematics of which we find evidence at least on scales of a few arcmin. Therefore we need a better understanding of higher order correlations of cosmic shear and their systematics to confidently apply them as cosmological probes.

**Key words:** gravitational lensing: weak – methods: statistical – cosmology: observations – dark matter.

## 1 INTRODUCTION

The statistics of the distribution of matter on large cosmological scales, when combined with other cosmological probes, is a powerful tool to discriminate between different cosmological models (e.g. Dodelson 2003; Laureijs et al. 2011). Gravitational lensing is a technique to assess the mass distribution in the Universe in a way that is independent of the exact nature of dark matter and its dynamical state (Bartelmann & Schneider 2001, for an extensive review). One of the consequences of gravitational lensing is cosmic shear, which we statistically infer from correlations between shapes of distant galaxies (see Schneider 2006; Kilbinger 2014, for a recent review on weak gravitational lensing). The correlations between

* E-mail: psimon@astro.uni-bonn.de

shapes of galaxy pairs give a measurement of the projected matter density power spectrum, which in turn constrains the geometry of the Universe and the growth of structure.

The most recent cosmological constraints from cosmic shear are reported by Fu et al. (2014, hereafter F14), Kilbinger et al. (2013), Kitching et al. (2014), Benjamin et al. (2013), and Heymans et al. (2013) where the authors analyse the latest data release by the Canada–France–Hawaii Telescope Lensing Survey (CFHTLenS) team.[1] This lensing catalogue builds upon the Canada–France–Hawaii Telescope Legacy Survey (CFHTLS), which represents together with the Red Cluster Sequence Lensing Survey[2] the state-of-the-art of gravitational lensing surveys from the ground. A preliminary weak lensing analysis of the CFHTLS has been presented earlier in Hoekstra et al. (2006), Semboloni et al. (2006), Benjamin et al. (2007), and Fu et al. (2008). Since then, however, the CFHTLenS data have significantly improved in terms of the characterization of the residual systematics and the estimation of galaxy redshifts, making the full scientific potential of weak lensing a reality (Heymans et al. 2012; Hildebrandt et al. 2012; Erben et al. 2013; Gillis et al. 2013; Simon et al. 2013; Simpson et al. 2013; van Waerbeke et al. 2013; Velander et al. 2014).

While current studies mainly focus on the two-point correlations in the cosmic shear field, higher order statistics contain more information, and this can improve constraints on cosmological models (Bernardeau, van Waerbeke & Mellier 1997, 2003; van Waerbeke, Bernardeau & Mellier 1999; Schneider & Lombardi 2003; Takada & Jain 2003; Kilbinger & Schneider 2005; Schneider, Kilbinger & Lombardi 2005; Bergé, Amara & Réfrégier 2010; Vafaei et al. 2010; Kayo, Takada & Jain 2013). For the ongoing wide field surveys, such as the Kilo Degree Survey (KiDS),[3] the Dark Energy Survey (DES),[4] the Hyper Suprime-Cam survey (HSC),[5] and future surveys such as the Large Synoptic Survey Telescope (LSST)[6] and *Euclid*,[7] the statistical power of the three-point shear statistics alone is comparable to that of two-point shear statistics (Vafaei et al. 2010; Kayo et al. 2013). Therefore, prospects on obtaining cosmological information from third-order shear statistics are high.

On the observational side, early attempts to measure the three-point shear statistics were carried out by Pen et al. (2003) and Jarvis, Bernstein & Jain (2004). These two studies were performed using small data sets and shape measurement algorithms that are not as robust as algorithms today. While in both studies a signal was detected, the results were strongly affected by residual point spread function (PSF) systematics. More recently, Semboloni et al. (2011) used high-quality space-based data, the *Hubble Space Telescope* (*HST*)/Cosmic Evolution Survey (COSMOS) data set, to perform a measurement of three-point shear statistics that did not show evidence of residual systematics; however, the analysis was limited to 1.6 deg$^2$ of the COSMOS data. The latest successful measurements of third-order shear statistics have been performed by F14 and van Waerbeke et al. (2013) based on the CFHTLenS data set. These two different approaches, shear correlation functions and moments in the reconstructed lensing mass map, are complementary and are sensitive to different residual systematics.

The interpretation of these statistics is still plagued and possibly limited by theoretical uncertainties. A correct interpretation of this signal can only be performed by accurately modelling the evolution of the matter bispectrum in the non-linear regime. Analytical fitting formulae such as Scoccimarro & Couchman (2001) are only accurate at the 10–20 per cent level (van Waerbeke et al. 2001; Semboloni et al. 2011; Harnois-Déraps, Vafaei & van Waerbeke 2012). Alternative approaches based on the halo model also have a limited accuracy (Valageas & Nishimichi 2011a,b; Kayo et al. 2013).

Moreover, other phenomena are expected to affect the measured signal, such as baryonic physics in the non-linear regime, intrinsic alignments (IAs) of source galaxies, and source–lens clustering. These phenomena have not yet been extensively studied and are uncertain (Hamana et al. 2002; Semboloni et al. 2008, 2011; F14; Harnois-Déraps et al. 2014).

Improvements of both the theoretical cosmological models and the reduction of systematics in observational data are only two pillars of a successful exploitation of the plentiful cosmological information in the higher order shear statistics. The success will also depend on realistic models of statistical uncertainties in the shear correlation estimators. For this, a Gaussian likelihood is typically used in the statistical analysis, such as in F14, whereas at least for second-order cosmic shear statistics there is evidence in favour of more complex models (Hartlap et al. 2009; Keitel & Schneider 2011; Sato, Ichiki & Takeuchi 2011; Wilking & Schneider 2013). For this paper, we hypothesize that a Gaussian model for the data likelihood of third-order shear correlations possibly yields biased results for cosmological parameters. We motivate this by our observation in Section 4 that the distribution of the estimates in simulations of the CFHTLenS data exhibits a non-Gaussian distribution on angular scales of around 10–30 arcmin, violating the assumption of Gaussian noise. To test our hypothesis for CFHTLenS data we compare the cosmological constraints obtained from measurements of the third moment of the aperture mass when based on Gaussian versus non-Gaussian likelihoods (Schneider et al. 1998, 2005). The CFHTLenS data are briefly summarized in Section 2. Our first analysis uses a commonly used Gaussian likelihood as in F14, whereas the second analysis uses a non-Gaussian model. Our estimator of the third-order shear statistics is detailed in Section 3. For the cosmology, we assume a flat Λ cold dark matter (ΛCDM) model with the matter density parameter $\Omega_m$ and the amplitude of fluctuations in the matter density field $\sigma_8$ as free parameters; a flat ΛCDM model is strongly supported by recent constraints from the cosmic microwave background (CMB; Komatsu et al. 2009; Planck Collaboration XVI 2014). Based on our new technique in Section 5, we construct the non-Gaussian likelihood from a set of simulated measurements. We present the results in Section 6 and discuss them in Section 7. In comparison to the two-point systematics analysis of Heymans et al. (2012, hereafter H12), we perform new tests for third-order shear systematics of CFHTLenS that we present in Section 4.2 and in Appendix A.

## 2 DATA

### 2.1 CFHTLenS

The CFHTLS-Wide survey area is divided into four independent fields (W1, W2, W3, W4), with a total area of 154 deg$^2$, observed in the five optical bands $u^*, g', r', i', z'$. Each field is a mosaic of several MEGACAM fields, called pointings. More details about the data set itself are given in Erben et al. (2013). The procedure for the shape measurements using LENSFIT can be found in Miller et al. (2007,

---

[1] http://www.cfhtlens.org
[2] http://www.rcslens.org
[3] http://kids.strw.leidenuniv.nl (de Jong et al. 2013).
[4] http://www.darkenergysurvey.org (The Dark Energy Survey Collaboration 2005).
[5] http://www.subarutelescope.org/Projects/HSC (Miyazaki et al. 2012).
[6] http://www.lsst.org (Abell et al. 2009).
[7] http://sci.esa.int/euclid (Laureijis R. et al. 2011).

2013) and Kitching et al. (2008), and the photometric redshifts are described in Hildebrandt et al. (2012).

A description of the CFHTLenS shear catalogue, and the residual systematics based on the shear two-point correlation function, is given in H12.

For the measurement of the three-point shear statistics presented in this paper, we use galaxies from the 129 pointings selected by H12, with $0.2 < z_{phot} < 1.3$ and $i' < 24.7$. The mosaic for each field has been constructed by merging the single pointings, so that overlaps are eliminated, and each galaxy appears only once. Each field is projected on the tangential plane centred in the middle using a gnomonic projection (see e.g. Calabretta & Greisen 2000). Three-point shear correlation functions are measured for each of the four fields, i.e. not for individual pointings, using for each galaxy the final Cartesian coordinates $(x, y)$ (flat sky approximation), the ellipticity $(\epsilon_1, \epsilon_2)$, and weights $w$ provided by LENSFIT.

In order to interpret the shear signal we need to know the redshift distribution of the sources. The redshift probability distribution function (PDF) of each galaxy in the CFHTLenS catalogues is sampled in 70 redshift bins of width 0.05 between 0 and 3. We obtain the source redshift distribution of the full data set by stacking the distributions of all galaxies. However, since each galaxy in our sample is weighted according to $w$ when we compute the shear signal, we need to weight the PDF of each galaxy to obtain the effective redshift distribution of the sources, $p_z(z)$. This technique is explained and tested in Benjamin et al. (2013). The final redshift distribution, shown in Fig. 1, has a mean redshift of $\bar{z}_{phot} = 0.74$, and it is sampled in 30 steps between redshift 0 and 3.

### 2.2 Clone simulations of CFHTLenS

The CFHTLenS clone is a mock survey in which the lensing signal obtained from $N$-body simulations is known, and the observational properties, such as galaxy position, ellipticity, magnitude, weight, are included such that the clone's are consistent with the data. In this paper, we use the CFHTLenS clone for various purposes. A thorough description of the dark-matter-only simulations can be found in Harnois-Déraps et al. (2012). These simulations have been constructed using the 5-year *Wilkinson Microwave Anisotropy Probe* (*WMAP*5)+supernovae (SN)+ baryon
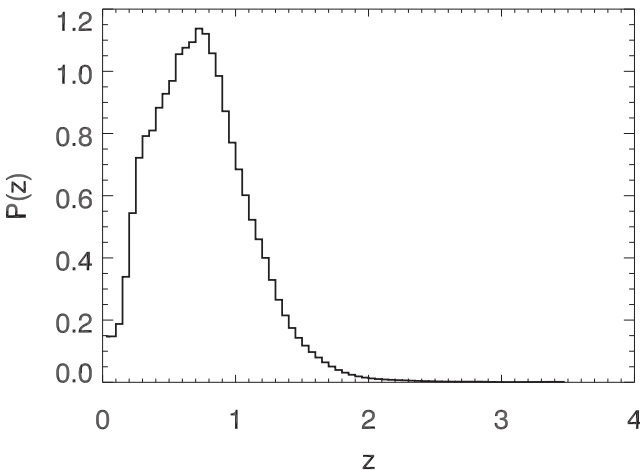


**Figure 1.** Source redshift distribution $p_z(z)$ obtained by stacking the probability densities of all galaxies with $0.2 < z_{phot} < 1.3$, $i' < 24.7$, weighted by the LENSFIT weight $w$. This distribution is used here to construct a forecast of the cosmological shear signal for a *WMAP*5 cosmology.

acoustic oscillations (BAO) cosmology: $\{\Omega_m, \Omega_\Lambda, \Omega_b, n, h, \sigma_8\} = \{0.279, 0.721, 0.046, 0.96, 0.701, 0.817\}$ (Komatsu et al. 2009). Starting at an initial redshift of 200, the mass density in the simulation box is sampled at 26 different redshifts between $z = 3$ and 0. The density fields are collapsed along one of the Cartesian axes, and the resulting series of planes are used to generate shear, convergence, and mass maps inside the light cone. The 184 independent line-of-sights cover an area of 12.84 deg$^2$ each and have been populated with sources using the same redshift distribution and galaxy density as in the CFHTLenS observations.

The clone does not include density fluctuations larger than the simulation box, and this is known to affect the covariance estimated from these simulated maps. These missing supersurvey modes propagate in many ways in the shear covariance (Li, Hu & Takada 2014). Our measurement, however, is very weakly impacted by these for two reasons. First, our shear aperture statistics uses only aperture scales up to 30 arcmin, which is well below the maximum usable scale of 70 arcmin. This makes the *finite support effect* described in Harnois-Déraps & van Waerbeke (2014) at most a 5 per cent deficit on the error bar of the largest angles. Second, we must also examine the contribution from the *halo sampling variance*, *beat coupling* and *dilation*, which causes the small-scale clustering variance to be underestimated (Hamilton, Rimes & Scoccimarro 2006; Rimes & Hamilton 2006). As summarized in Harnois-Déraps & van Waerbeke (2014), simulation boxes of 500 $h^{-1}$ Mpc miss about 90 per cent of the non-Gaussian part of the variance at $z = 0$. We can expect that the clone misses even more due to the smaller size of the box. However, weak lensing projects many scales on to the same angular measurement, which dramatically decreases the non-Gaussian contribution to the error bar. In this case, the most important contribution to the supersample covariance comes from the *halo sampling variance*, which peaks at small scales. As argued in Kilbinger et al. (2013), this causes the small-scale covariance to be underestimated by less than 10 per cent, hence we do not explicitly correct for supersurvey modes in the clone.

## 3 THREE-POINT SHEAR STATISTICS

### 3.1 Definition of statistics

In this section, we briefly outline the relation between cosmic shear and the statistics of the matter density fluctuation. The matter density field at comoving position $\chi$ and at redshift $z$ is $\rho(\chi; z) \equiv \bar{\rho}(z)[1 + \delta(\chi; z)]$, where $\delta$ is the density contrast and $\bar{\rho}(z)$ the average density at redshift $z$. The power spectrum $P(k; z)$ and the bispectrum $B(k_1, k_2, k_3; z)$ are defined by the correlators

$$\left\langle \tilde{\delta}(\boldsymbol{k}_1; z)\tilde{\delta}(\boldsymbol{k}_2; z) \right\rangle \equiv (2\pi)^3 \delta_D(\boldsymbol{k}_1 + \boldsymbol{k}_2)P(k_1; z) \qquad (1)$$

and

$$\left\langle \tilde{\delta}(\boldsymbol{k}_1; z)\tilde{\delta}(\boldsymbol{k}_2; z)\tilde{\delta}(\boldsymbol{k}_3; z) \right\rangle$$
$$\equiv (2\pi)^3 \delta_D(\boldsymbol{k}_1 + \boldsymbol{k}_2 + \boldsymbol{k}_3)B(k_1, k_2, k_3; z) \qquad (2)$$

of the Fourier transform $\tilde{\delta}(\boldsymbol{k}_i; z)$ of the density contrast $\delta$ for the three-dimensional (3D) wavenumber $\boldsymbol{k}_i$ at redshift $z$.

We apply a flat-sky approximation in the following. Let $\chi_\perp$ be the two-dimensional (2D) vector that we obtain by projecting $\chi$ on to the tangential plane on the celestial sphere that is defined by the line-of-sight direction; the $x$- and $y$-coordinates of $\chi_\perp$ are $x$ and $y$, respectively. The complex shear $\gamma = \gamma_1 + i\gamma_2$ and the convergence $\kappa$ at angle $s$ are both functions of the second-order derivatives of the gravitational potential $\phi(\chi_\perp; \chi)$ at $\chi_\perp := s f_K(\chi)$ with $f_K(\chi)$ being

the comoving angular diameter distance at radial distance $\chi = |\boldsymbol{\chi}|$. Following Schneider et al. (1998) we find at angle $\boldsymbol{s}$ in the tangential plane:

$$\kappa(\boldsymbol{s}) = \frac{3\Omega_{\mathrm{m}} H_0^2}{2c^2} \int_0^{\chi_{\mathrm{h}}} \mathrm{d}\chi \, \frac{g(\chi) f_{\mathrm{K}}(\chi)}{a(\chi)} (\partial_x^2 + \partial_y^2)\phi\left(\boldsymbol{\chi}_{\perp}; \chi\right), \qquad (3)$$

$$\gamma_1(\boldsymbol{s}) = \frac{3\Omega_{\mathrm{m}} H_0^2}{2c^2} \int_0^{\chi_{\mathrm{h}}} \mathrm{d}\chi \, \frac{g(\chi) f_{\mathrm{K}}(\chi)}{a(\chi)} (\partial_x^2 - \partial_y^2)\phi\left(\boldsymbol{\chi}_{\perp}; \chi\right), \qquad (4)$$

$$\gamma_2(\boldsymbol{s}) = \frac{3\Omega_{\mathrm{m}} H_0^2}{2c^2} \int_0^{\chi_{\mathrm{h}}} \mathrm{d}\chi \, \frac{g(\chi) f_{\mathrm{K}}(\chi)}{a(\chi)} 2\partial_x \partial_y \phi\left(\boldsymbol{\chi}_{\perp}; \chi\right), \qquad (5)$$

where $H_0$ is the Hubble constant, $\Omega_{\mathrm{m}}$ is the matter density parameter, $c$ is the vacuum speed of light, $a$ is the cosmological scale factor, $\chi_{\mathrm{h}}$ is the size of the Hubble horizon, and $p_{\chi}(\chi)\mathrm{d}\chi$ in

$$g(\chi) := \int_{\chi}^{\chi_{\mathrm{h}}} \mathrm{d}\chi' p_{\chi}(\chi') \frac{f_{\mathrm{K}}(\chi' - \chi)}{f_{\mathrm{K}}(\chi')} \qquad (6)$$

describes the distribution of sources per distance interval $\mathrm{d}\chi$, or per redshift interval in the case of $p_z(z)\mathrm{d}z$.

In the weak lensing regime of cosmic shear, we find $\kappa \ll 1$ and $|\gamma| \ll 1$ such that the observable galaxy ellipticity $\boldsymbol{\epsilon} = \epsilon_1 + \mathrm{i}\epsilon_2$ becomes an unbiased estimator of the galaxy shear to first approximation, i.e. $\langle \boldsymbol{\epsilon} \rangle = \boldsymbol{\gamma}$. In addition, by assuming that galaxies are randomly oriented intrinsically, the Fourier transform of the angular correlation $\langle \epsilon_i \epsilon_j^* \rangle = \langle \gamma_i \gamma_j^* \rangle = \langle \kappa_i \kappa_j \rangle$ between the ellipticities of pairs of galaxies $i, j$ can be interpreted as a direct measure of the matter power spectrum in projection on the sky,

$$P_{\kappa}(\ell) = P_{\gamma}(\ell) = \frac{9\Omega_{\mathrm{m}}^2 H_0^4}{4c^4} \int_0^{\chi_{\mathrm{h}}} \mathrm{d}\chi \, \frac{g^2(\chi)}{a^2(\chi)} P\left(\frac{\ell}{f_{\mathrm{K}}(\chi)}; z(\chi)\right). \qquad (7)$$

By $\boldsymbol{\gamma}^*$ we denote the complex conjugate of $\boldsymbol{\gamma}$. The angular power spectrum $P_{\kappa}(\ell)$ of $\kappa$ is defined by

$$\langle \tilde{\kappa}(\boldsymbol{\ell}_1)\tilde{\kappa}(\boldsymbol{\ell}_2) \rangle = (2\pi)^2 \delta_{\mathrm{D}}(\boldsymbol{\ell}_1 + \boldsymbol{\ell}_2) P_{\kappa}(\ell_1) \qquad (8)$$

for the angular wavenumber $\ell$.

A similar relation exists between the angular bispectrum $B_{\kappa}$ of $\kappa$,

$$\langle \tilde{\kappa}(\boldsymbol{\ell}_1)\tilde{\kappa}(\boldsymbol{\ell}_2)\tilde{\kappa}(\boldsymbol{\ell}_3) \rangle = (2\pi)^2 \delta_{\mathrm{D}}(\boldsymbol{\ell}_1 + \boldsymbol{\ell}_2 + \boldsymbol{\ell}_3) B_{\kappa}(\ell_1, \ell_2, \ell_3), \qquad (9)$$

attainable through the correlation of three galaxy ellipticities, and the projected matter bispectrum

$$B_{\kappa}(\ell_1, \ell_2, \ell_3) = \frac{27 H_0^6 \Omega_{\mathrm{m}}^3}{8c^6} \int \mathrm{d}\chi \, \frac{g^3(\chi)}{f_{\mathrm{K}}(\chi) a^3(\chi)}$$
$$\times B\left(\frac{\ell_1}{f_{\mathrm{K}}(\chi)}, \frac{\ell_2}{f_{\mathrm{K}}(\chi)}, \frac{\ell_3}{f_{\mathrm{K}}(\chi)}; z(\chi)\right) \qquad (10)$$

(Bernardeau et al. 1997; Schneider et al. 1998). In contrast to second-order statistics, four independent correlation functions of the third-order statistics can be defined. We utilize the representation of the correlator in terms of its natural components as advocated by Schneider & Lombardi (2003). Let $\boldsymbol{r}$, $\boldsymbol{r} + \boldsymbol{s}$, and $\boldsymbol{r} + \boldsymbol{t}$ be the angular positions of three galaxies, while $\alpha$ denotes the angle between the $x$-axis and $\boldsymbol{s}$. The natural components are then given by

$$\Gamma_0(s, t') = \left\langle \gamma(\boldsymbol{r})\gamma(\boldsymbol{r} + \boldsymbol{s})\gamma(\boldsymbol{r} + \boldsymbol{t})\mathrm{e}^{-6\mathrm{i}\alpha} \right\rangle, \qquad (11)$$

$$\Gamma_1(s, t') = \left\langle \gamma^*(\boldsymbol{r})\gamma(\boldsymbol{r} + \boldsymbol{s})\gamma(\boldsymbol{r} + \boldsymbol{t})\mathrm{e}^{-2\mathrm{i}\alpha} \right\rangle, \qquad (12)$$

$$\Gamma_2(s, t') = \left\langle \gamma(\boldsymbol{r})\gamma^*(\boldsymbol{r} + \boldsymbol{s})\gamma(\boldsymbol{r} + \boldsymbol{t})\mathrm{e}^{-2\mathrm{i}\alpha} \right\rangle, \qquad (13)$$

$$\Gamma_3(s, t') = \left\langle \gamma(\boldsymbol{r})\gamma(\boldsymbol{r} + \boldsymbol{s})\gamma^*(\boldsymbol{r} + \boldsymbol{t})\mathrm{e}^{-2\mathrm{i}\alpha} \right\rangle, \qquad (14)$$

where $s = \sqrt{\boldsymbol{s}\boldsymbol{s}^*}$ of $\boldsymbol{s}$ and $t' = \boldsymbol{t}\boldsymbol{s}^*/s$. In equations (11)–(14), the ensemble averages are performed over triangles invariant under translation and rotation. These triangles can hence be characterized by three real-valued variables $s$ and $t' = t_1' + \mathrm{i}t_2'$. The component $\Gamma_0$ is invariant under a parity transformation, whereas $\Gamma_{1,2,3}$ are not (Schneider & Lombardi 2003).

For our analysis, we integrate the natural components to obtain an alternative third-order statistic of shear, the third moment of the aperture mass (Schneider et al. 1998),

$$M_{\mathrm{ap}}(\theta) = \int \mathrm{d}^2 r \, U_{\theta}(|\boldsymbol{r}|)\kappa(\boldsymbol{r}), \qquad (15)$$

for an aperture filter $U_{\theta}(r)$ and a triplet $(\theta_1, \theta_2, \theta_3)$ of aperture radii,

$$\left\langle M_{\mathrm{ap}}^3(\theta_1, \theta_2, \theta_3) \right\rangle$$
$$= \int \left\{ \prod_{j=1}^3 \frac{\mathrm{d}^2 r_j \mathrm{d}^2 \ell_j U_{\theta_j}(|\boldsymbol{r}_j|)\mathrm{e}^{\mathrm{i}\boldsymbol{r}_j \cdot \boldsymbol{\ell}_j}}{(2\pi)^2} \right\} \langle \tilde{\kappa}(\boldsymbol{\ell}_1)\tilde{\kappa}(\boldsymbol{\ell}_2)\tilde{\kappa}(\boldsymbol{\ell}_3) \rangle \qquad (16)$$

(Pen et al. 2003; Jarvis et al. 2004; Schneider et al. 2005). Roughly speaking, $M_{\mathrm{ap}}(\theta)$ is the $U_{\theta}$-smoothed convergence field at $\boldsymbol{r} = 0$, and $\langle M_{\mathrm{ap}}^3(\theta_1, \theta_2, \theta_3) \rangle$ is the $U_{\theta}$-smoothed version of the correlator $\langle \tilde{\kappa}(\boldsymbol{\ell}_1)\tilde{\kappa}(\boldsymbol{\ell}_2)\tilde{\kappa}(\boldsymbol{\ell}_3) \rangle$, which is a measure of the projected matter bispectrum in equation (10). In particular, by choosing an exponential aperture filter as in van Waerbeke (1998),

$$U_{\theta}(r) = \frac{1}{2\pi\theta^2}\left(1 - \frac{r^2}{2\theta^2}\right)\mathrm{e}^{-\frac{1}{2}(\frac{r}{\theta})^2}, \qquad (17)$$

the relation between three-point correlation functions and the third moment of $\langle M_{\mathrm{ap}}^3 \rangle$ is relatively simple. Note that our filter has been rescaled by $2\sqrt{2}\theta$ in comparison to van Waerbeke (1998). Our filter peaks at $\ell = \sqrt{2}/\theta \approx 4862\,(\theta/1')^{-1}$ in wavenumber space.

### 3.2 Model of the matter bispectrum

Equations (9), (10), and (16) establish an explicit relation between $B(k_1, k_2, k_3; z)$ and the third moment $\langle M_{\mathrm{ap}}^3 \rangle$. Thus, in order to predict $\langle M_{\mathrm{ap}}^3 \rangle$ we need to model the bispectrum of matter fluctuations. It is important that the bispectrum model captures the mode coupling beyond perturbation theory, since our CFHTLenS measurements are probing the non-linear regime of $k \sim 0.1$-$10\,h\,\mathrm{Mpc}^{-1}$. To this end, we employ the bispectrum fit of Scoccimarro & Couchman (2001, hereafter SC01). The work of SC01 produced an analytical fit to the non-linear evolution of the bispectrum based on a suite of cold dark matter $N$-body simulations that was available at that time. The accuracy of this fit is limited by the accuracy of the $N$-body simulations in their study and by the fact that the effect of baryons on the small-scale clustering of matter is not included. In short, the fit of SC01 consists of a refinement lowest order perturbation theory:

$$B(k_1, k_2, k_3; z) = 2F(\boldsymbol{k}_1, \boldsymbol{k}_2; z)P(k_1; z)P(k_2; z) + \text{cycl.}, \qquad (18)$$

where cycl. indicates a cyclic permutation of the indices. SC01 express the non-linear extension of the mode coupling factors

$F(\boldsymbol{k}_1, \boldsymbol{k}_2; z)$ as

$$F(\boldsymbol{k}_1, \boldsymbol{k}_2, z) = \frac{5}{7} a(n, k_1; z) a(n, k_2; z)$$
$$+ \frac{1}{2} \frac{\boldsymbol{k}_1 \cdot \boldsymbol{k}_2}{k_1 k_2} \left( \frac{k_1}{k_2} + \frac{k_2}{k_1} \right) b(n, k_1; z) b(n, k_2; z)$$
$$+ \frac{2}{7} \left( \frac{\boldsymbol{k}_1 \cdot \boldsymbol{k}_2}{k_1 k_2} \right)^2 c(n, k_1; z) c(n, k_2; z), \qquad (19)$$

where the coefficients

$$a(n, k; z) = \frac{1 + \sigma_8(z)^{-0.2} [0.7 Q_3(n)]^{1/2} (q[z]/4)^{n+3.5}}{1 + (q[z]/4)^{n+3.5}}, \qquad (20)$$

$$b(n, k; z) = \frac{1 + 0.4(n + 0.3) q[z]^{n+3}}{1 + q[z]^{n+3.5}}, \qquad (21)$$

$$c(n, k; z) = \frac{1 + 4.5/[1.5 + (n + 3)^4](2q[z])^{n+3}}{1 + (2q[z])^{n+3.5}} \qquad (22)$$

have been fitted to the $N$-body simulations with

$$Q_3(n) = \frac{4 - 2^n}{1 + 2^{n+1}}. \qquad (23)$$

Here $\sigma_8(z)$ is the standard deviation of matter density fluctuations within a sphere of radius $8\,h^{-1}$ Mpc linearly devolved from zero to redshift $z$, and $n$ is the spectral index of the primordial power spectrum. The time dependence of $F(\boldsymbol{k}_1, \boldsymbol{k}_2; z)$ is given by both the evolution of $\sigma_8(z)$ and the function $q[z] = k/k_{\rm nl}[z]$ where $4\pi k_{\rm nl}[z]^3 P_{\rm lin}(k_{\rm nl}[z]; z) = 1$ defines the wavenumber $k_{\rm nl}[z]$ of the non-linear regime at redshift $z$, $P_{\rm lin}(k; z)$ denotes the linear matter power spectrum.

SC01 showed that this approximation is accurate to within 15 per cent up to $k$ of a few $h\,\mathrm{Mpc}^{-1}$. van Waerbeke et al. (2001) compared the third-order moments of the projected density field measured directly on simulated $\kappa$ maps with predictions obtained using the fitting formula. They found a similar accuracy. In agreement with these previous results, Semboloni et al. (2011) found that this approximation systematically underestimates $\langle M_{\rm ap}^3 \rangle$ on small angular scales. A different approach to compute the bispectrum has been recently suggested by Valageas & Nishimichi (2011a,b). It uses a combination of perturbation theory and the halo model. This approach is promising but its performance depends on the accuracy of the halo model which is in general still limited. Moreover, none of these approximations accounts for the potentially large effects from baryonic physics (Semboloni et al. 2011). Overall, the accuracy of bispectrum predictions is therefore still an open issue. Current models cannot claim an accuracy better than ~20 per cent which we include in our cosmological analysis. Consequently further improvements in modelling are necessary in the future, which is beyond the scope of this work.

We note here that the coefficients of SC01 have recently been updated by Gil-Marin et al. (2012). Our analysis does not include this update as the corrections are smaller than the 20 per cent model error that we include in our analysis, and as such this update would not impact our results. Moreover, as non-linear power spectrum $P(k; z)$ in equation (18) we use the model of Smith et al. (2003) with the transfer function of Eisenstein & Hu (1998). As recently reported in Harnois-Déraps et al. (2014), this model lacks power on small scales in comparison to $N$-body simulations. As shown in Section 4.1, however, this bias is negligible on the angular scales that we exploit for our analysis.

### 3.3 Estimators of the natural components

The measurement of the third-order moment of the aperture mass statistics, $\langle M_{\rm ap}^3(\theta_1, \theta_2, \theta_3) \rangle$, is performed using the same procedure described in Semboloni et al. (2011) and in the recent F14 analysis (see their section 2.3). This procedure consists of reconstructing $\langle M_{\rm ap}^3 \rangle$ by numerical integration of estimates of the natural components $\boldsymbol{\Gamma}_i$.

For the estimators of the natural components equations (11)–(14), we bin the products of three source ellipticities of similar triangle configurations. One possible choice is to bin the triangles according to their values of $(s, t_1', t_2')$. However, Jarvis et al. (2004) suggested a more suitable binning scheme. Given three sides $s$, $t$, $d_1$ with $s < t < d_1$, the following variables are defined:

$$d = s, \quad d_{\min} < d < d_{\max}, \qquad (24)$$

$$u = s/t, \quad 0 < u < 1, \qquad (25)$$

$$v = \pm \frac{d_1 - t}{s}, \quad -1 < v < 1. \qquad (26)$$

Assigning a sign to $v$ keeps track of the triangle orientation: if $t_x' = t_x$ (that is $s_x > 0$, i.e. the triangle is clockwise oriented), then $v > 0$, otherwise $v < 0$. The limits $d_{\min}$ and $d_{\max}$ are the minimal and maximal lengths for the smallest triangle side $s$ and define the range on which the natural components are sampled. For the CFHTLenS fields, $d_{\min}$ is set to 9 arcsec in order to avoid bias from close galaxies pairs with overlapping isophotes. The maximum separation is set to $d_{\max} = 400$ arcmin which means that $\langle M_{\rm ap}^3 \rangle$ can be reconstructed up to angular scales $\lesssim 100$ arcmin. We compute the correlation function of the galaxy triplets by a TREE-code approach, similar to the one suggested by Zhang & Pen (2005). In our implementation of the tree code, we require $(S_1 + S_2)/D < 0.1$ as criterion for stopping a deeper search into the tree; $S_1$ and $S_2$ are the sizes of any pair of tree nodes belonging to a node triplet, and $D$ is the distance between the centres of the nodes.

In the case of the CFHTLenS catalogue, it is necessary to account for a multiplicative correction factor $m(\nu_{\rm S/N}, r_{\rm gal})$ assigned to each galaxy (H12; Miller et al. 2013). The correction factor depends on the galaxy signal-to-noise ratio (S/N) $\nu_{\rm S/N}$ and size $r_{\rm gal}$. According to Miller et al. (2013), for an average shear $\langle \gamma_i \rangle$ the corrected estimate of the $i$-component is given by

$$\langle \gamma_i \rangle_{\rm cal} = \frac{\langle \gamma_i \rangle}{\langle 1 + m \rangle}, \quad \text{with } i = 1, 2, \qquad (27)$$

where $\langle \dots \rangle$ indicates ensemble weighted averages for $n_{\rm gal}$ galaxies defined using the LENSFIT weights $w$, namely

$$\langle \gamma_i \rangle = \left( \sum_{a=1}^{n_{\rm gal}} w_a \right)^{-1} \sum_{a=1}^{n_{\rm gal}} \epsilon_{i,a} w_a, \qquad (28)$$

$$\langle 1 + m \rangle = \left( \sum_{a=1}^{n_{\rm gal}} w_a \right)^{-1} \sum_{a=1}^{n_{\rm gal}} w_a (1 + m_a(\nu_{\rm S/N}, r_{\rm gal})). \qquad (29)$$

The extension of this calibration scheme to the three-point shear statistics is straightforward:

$$\langle \gamma_i \gamma_j \gamma_k \rangle_{\rm cal} = \frac{\sum\limits_{\rm abc} \epsilon_{i,a} \epsilon_{j,b} \epsilon_{k,c} w_a w_b w_c}{\sum\limits_{\rm abc} w_a w_b w_c (1 + m_a)(1 + m_b)(1 + m_c)}, \qquad (30)$$

where the sum is over all triplets $\widehat{a, b, c}$ belonging to a bin and $i, j, k = 1, 2$ denote the shear components. This correction is applied to our practical estimators of the natural components,

$$\mathbf{\Gamma}_0(s, t') = \frac{\sum_{\widehat{a,b,c}} w_a w_b w_c \epsilon_a \epsilon_b \epsilon_c e^{-6i\alpha_b}}{\sum_{\widehat{a,b,c}} w_a w_b w_c (1 + m_a)(1 + m_b)(1 + m_c)} \quad (31)$$

and

$$\mathbf{\Gamma}_1(s, t') = \frac{\sum_{\widehat{a,b,c}} w_a w_b w_c \epsilon_a^* \epsilon_b \epsilon_c e^{-2i\alpha_b}}{\sum_{\widehat{a,b,c}} w_a w_b w_c (1 + m_a)(1 + m_b)(1 + m_c)}. \quad (32)$$

We obtain the remaining two other estimators $\mathbf{\Gamma}_{2,3}(s, t')$ by cyclic permutations of the triangle parameters (Schneider & Lombardi 2003).

## 3.4 Estimators of modes of the aperture statistics

In practice, we encounter four distinct modes of the aperture statistics due to the possible presence of B-modes in the shear field. Known sources of B-modes are systematics due to residuals in the PSF correction or IAs between the sources (e.g. Heavens, Refregier & Heymans 2000; Kitching et al. 2012). Even without these systematics higher order effects such as lens coupling and corrections beyond the Born approximation give rise to B-modes, however, much smaller than the amplitude of the E-modes (Schneider et al. 1998; Cooray & Hu 2002; Hirata & Seljak 2003).

For the aperture mass of an aperture centred on the origin $r = 0$, the formal separation between E- and B-modes is given by

$$M(\theta) = M_{\rm ap}(\theta) + iM_\perp(\theta)$$
$$= -\int d^2r\, Q_\theta(|\mathbf{r}|)\gamma(\mathbf{r})e^{-2i\phi}, \quad (33)$$

where the imaginary part $M_\perp(\theta)$ is the B-mode of the aperture mass, the real part $M_{\rm ap}(\theta)$ is the E-mode of equation (15), $\phi$ is the polar angle of $\mathbf{r}$, and

$$Q_\theta(x) = \left( \frac{2}{x^2} \int_0^x ds\, s U_\theta(s) \right) - U_\theta(x) \quad (34)$$

is the filter of the shear field that corresponds to $U_\theta$. We denote by $M^*(\theta)$ the complex conjugate of $M(\theta)$. To lowest order in $\delta\phi/c^2$, gravitational lensing can only produce E-modes, hence $M_\perp = 0$ in this regime. In this case, the third-order moment $\langle M_{\rm ap}^3(\theta_1, \theta_2, \theta_3) \rangle$ in equation (16) is given by the average $\langle M(\theta_1)M(\theta_2)M(\theta_3) \rangle$ over all available aperture positions. Generally, however, we have E/B mixing inside the correlator, giving rise to different modes of the statistics: the EEE, EEB, EBB, and BBB mode:

EEE : $\left\langle M_{\rm ap}^3(\theta_1, \theta_2, \theta_3) \right\rangle$

$$= \frac{1}{4}\mathrm{Re}\left( \langle \mathrm{M}^3(\theta_1, \theta_2, \theta_3) \rangle + \langle \mathrm{M}^2 M^*(\theta_1, \theta_2, \theta_3) \rangle \right.$$
$$\left. + \langle M^2 M^*(\theta_3, \theta_1, \theta_2) \rangle + \langle M^2 M^*(\theta_2, \theta_3, \theta_1) \rangle \right), \quad (35)$$

EEB : $\left\langle M_{\rm ap}^2 M_\perp(\theta_1, \theta_2, \theta_3) \right\rangle$

$$= \frac{1}{4}\mathrm{Im}\left( \langle \mathrm{M}^3(\theta_1, \theta_2, \theta_3) \rangle + \langle \mathrm{M}^2 M^*(\theta_3, \theta_1, \theta_2) \rangle \right.$$
$$\left. + \langle M^2 M^*(\theta_2, \theta_3, \theta_1) \rangle - \langle M^2 M^*(\theta_1, \theta_2, \theta_3) \rangle \right), \quad (36)$$

EBB : $\left\langle M_{\rm ap} M_\perp^2(\theta_1, \theta_2, \theta_3) \right\rangle$

$$= \frac{1}{4}\mathrm{Re}\left( - \langle \mathrm{M}^3(\theta_1, \theta_2, \theta_3) \rangle + \langle \mathrm{M}^2 M^*(\theta_1, \theta_2, \theta_3) \rangle \right.$$
$$\left. + \langle M^2 M^*(\theta_3, \theta_1, \theta_2) \rangle - \langle M^2 M^*(\theta_2, \theta_3, \theta_1) \rangle \right), \quad (37)$$

BBB : $\left\langle M_\perp^3(\theta_1, \theta_2, \theta_3) \right\rangle$

$$= \frac{1}{4}\mathrm{Im}\left( \langle \mathrm{M}^3(\theta_1, \theta_2, \theta_3) \rangle + \langle \mathrm{M}^2 M^*(\theta_1, \theta_2, \theta_3) \rangle \right.$$
$$\left. + \langle M^2 M^*(\theta_3, \theta_1, \theta_2) \rangle + \langle M^2 M^*(\theta_2, \theta_3, \theta_1) \rangle \right). \quad (38)$$

Note the order of the arguments $(\theta_1, \theta_2, \theta_3)$ in the previous equations. The actual cosmological signal EEE is the focus of this study. The modes EEB and BBB, or parity modes, are only present for parity violation (Schneider 2003), whereas the B-mode EBB may be the product of IAs of the galaxy ellipticities or an indicator of PSF systematics. To obtain the different modes, we estimate the two statistics $\langle M^3 \rangle$ and $\langle M^2 M^* \rangle$ from the measured natural components as in F14 (their equations 16 and 17).

Ideally, all four modes can be separated perfectly if the natural components are measured with infinite resolution and over the entire sky. However, the observed shear fields are finite, incomplete, and they are only sampled at the positions of sources. For second-order statistics, specially designed filters can be used to do this job; see for example Schneider, Eifler & Krause (2010) and references therein. For the third-order statistics in this study, on the other hand, this separation is currently not perfect. However, all these effects can be quantified and are much smaller than the expected signal. In addition, given the large errors in our measurements these inaccuracies are not important for this study. Therefore separating the signal into E-, B-, and parity components is nevertheless a very effective way to assess the cosmological origin of measured shear statistics.

## 4 SIMULATED DATA VERSUS MEASUREMENTS

### 4.1 Clone simulation

We measure the three-point shear signal on the 184 simulated 12.84 $\deg^2$ lines-of-sights from the CFHTLenS clone. For this purpose, we perform two separate measurements. Both sets of measurements are used for different purposes. First, for the *noise-free* sample, we analyse shear catalogues that assume intrinsically round sources. Second, for the *noisy* sample, we add ellipticity noise with an amplitude similar to the CFHTLenS data. The *noisy* sample is attained by adding a Gaussian random value with an average of zero and a one-dimensional (1D) dispersion of $\sigma_\epsilon = 0.28$ to a noise-free sample where this value is the measured ellipticity dispersion of the CFHTLenS including both intrinsic ellipticity dispersion and measurement noise; we do not include IAs. For each line-of sight, we measure the natural components $\mathbf{\Gamma}_i$ using the same binning and the same criteria we use on the CFHTLenS data. From the natural components, we then compute the third-order moments of the aperture mass by a numerical integration.

Fig. 2 verifies our method of computational analysis, supporting previous findings that the SC01 matter bispectrum is a reasonable fit to a dark-matter-only simulation of the standard cosmological model. Using the *noise-free* sample the figure displays the mean and standard error, due to cosmic variance, of the equilateral $\langle M_{\rm ap}^3(\theta_1 = \theta_2 = \theta_3) \rangle \equiv \langle M_{\rm ap}^3(\theta) \rangle$ obtained by averaging the 184 clone fields.
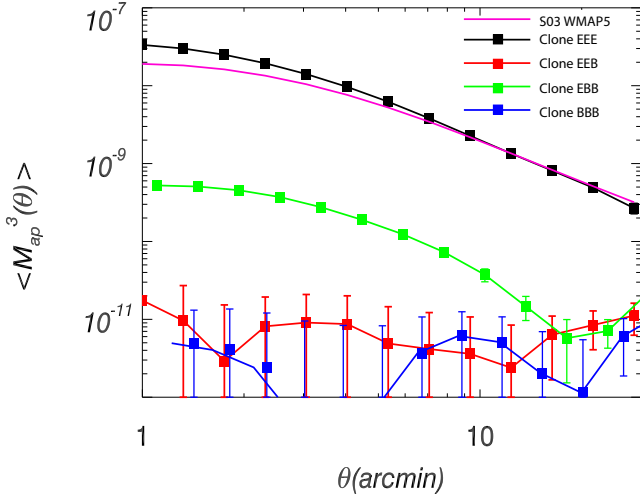
**Figure 2.** Measurement of the equilateral $\langle M_{ap}^3 \rangle$ for the *noise-free* data of the CFHTLenS clone. The signal has been divided in EEE (black solid squares), absolute values of the two parity modes BBB (blue) and EEB (red), and the B-mode EBB (green). Error bars represent the error on the average computed using the full suite of clone mock catalogues. For comparison, we show *WMAP*5 predictions done using Smith et al. (2003) and the fitting formula SC01 in Section 3.1.

The signal has been separated into E-, B-, and two parity modes. As mentioned before, due to E/B mixing of insufficiently sampled fields we expect a small level of B-modes in the estimators even for the pure cosmic shear fields as the ones in the simulation. We find that the BBB and EEB modes are consistent with zero, whereas the EBB mode exhibits a positive signal, albeit almost two orders of magnitude lower than the cosmological signal EEE. A possible explanation for this (negligible) EBB contamination, apart from the mixing, might be a numerical residual due to our numerical transformation from natural components to the aperture statistics. For reference, in the figure we also show the prediction of $\langle M_{ap}^3 \rangle$ for a *WMAP*5 cosmology and our SC01 model of the matter bispectrum. Moreover, we include the redshift distribution $p_z(z)$ of sources as shown in Section 2.1.

The agreement of the prediction and the measurement for the EEE signal is good overall. There is a discrepancy of about 10 per cent at around 5 arcmin increasing to 30 per cent at 1 arcmin. The discrepancy may be explained by the limited resolution of the simulations and the limited accuracy of our model of the non-linear matter power spectrum (Harnois-Déraps et al. 2012, 2014). In addition, there is a comparable inaccuracy in the non-linear regime due to baryonic physics that is not accounted for in the clone. We therefore take a conservative stand in our analysis and utilize only measurements on scales larger than 5 arcmin.

In contrast to our relatively good agreement between simulation and analytical model, Valageas, Sato & Nishimichi (2012) find that the SC01 model underestimates the power of a simulation by roughly a factor of 2 at 5 arcmin of $\langle M_{ap}^3 \rangle$ (their fig. 2; lower left-hand panel). However, the authors in this paper employ a polynomial filter that peaks at $\theta_{poly} \approx 5/\ell$, whereas our Gaussian aperture filter peaks at $\theta \approx \sqrt{2}/\ell$ (Schneider et al. 1998; Crittenden et al. 2002). This means that the corresponding scales of the polynomial filter are $\theta_{poly} \gtrsim 17.6$ arcmin for $\theta \gtrsim 5$ arcmin, where the agreement of SC01 is much better compared to the simulation. All the same, it is still possible that our good agreement between simulation and model is a coincidence that results from an offset
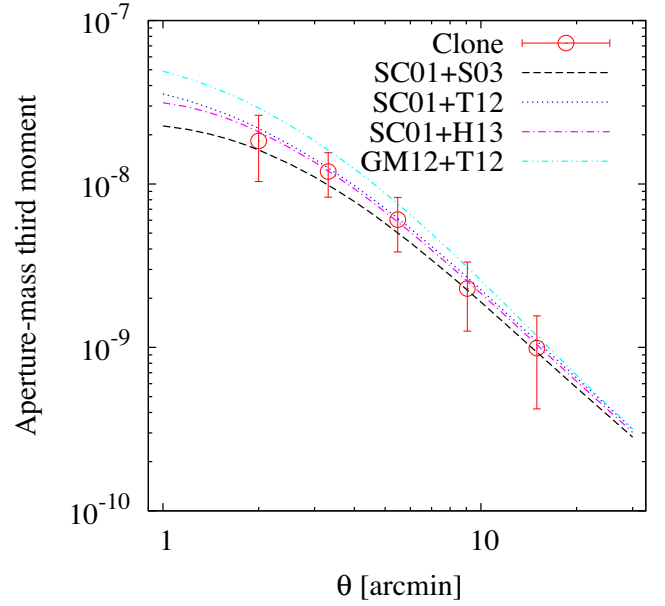


**Figure 3.** Data points of the equilateral $\langle M_{ap}^3 \rangle$ in the clone (open circles) in comparison to different analytical descriptions of the matter bispectrum (lines). The models are combinations of a fitting formula for the bispectrum with different prescriptions of the non-linear matter power spectrum; SC01: Scoccimarro & Couchman (2001); GM12: Gil-Marin et al. (2012); H13: Heitmann et al. (2014); T12: Takahashi et al. (2012); S03: Smith et al. (2003). We use SC01+S03 for the scope of this study (bottom black line). The figure is a reproduction of fig. A1 in F14.

of the clone power due to the limited resolution and volume of the simulation. In order to further investigate this, we reproduce the fig. A1 of our companion paper F14, see our Fig. 3. In this figure, we compare the clone measurements to a suit of recent, more accurate models of the matter bispectrum discussed in the literature (see figure caption). All these models agree with the clone within ~10 per cent for angular scales larger than or equal 5 arcmin (Gaussian aperture filter). In addition, our model SC01+S03 is below the amplitude of all recent models by about 10–20 per cent for scales larger than 5 arcmin (bottom black line). We therefore conclude that (i) analytical models of the matter bispectrum on the scales considered here rms vary within ~20 per cent, and (ii) the bispectrum power in the clone is sufficiently well described by SC01 on the angular scales that we consider by a cosmological analysis.

### 4.2 CFHTLenS measurement

In this section, we present our measurements of $\langle M_{ap}^3 \rangle$ in the CFHTLenS data. To start, in the left-hand panel of Fig. 4 we evaluate the difference between $\langle M_{ap}^3 \rangle$ as measured using all the 129 pointings to the same quantity measured excluding nine fields that fail our new residual systematics test in Appendix A. Our systematics test refines the tests done in H12 for third-order shear data. In the following, we refer to the 120 remaining fields as *pass fields*. These samples are utilized to constrain cosmological parameters. For Fig. 4 we calculate the error bars by rescaling the standard error of the mean in the 184 *noisy* clone simulation by the factor $\sqrt{A_{ratio}}$, where $A_{ratio} = 0.12$ is the area ratio between the *pass fields* and the simulation. The amplitude difference between the two measurements of $\langle M_{ap}^3 \rangle$ with and without the rejected nine fields are smaller than the statistical error. Nevertheless the two measurements are
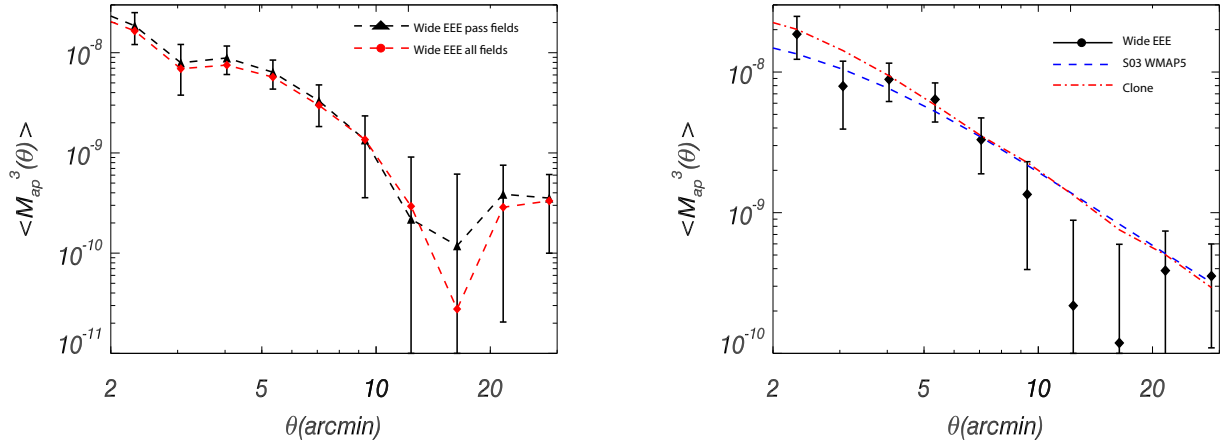
**Figure 4.** Left-hand panel: the black solid triangles show the equilateral $\langle M_{\mathrm{ap}}^3(\theta) \rangle$ computed using all the 120 CFHTLenS fields passing the systematic tests by H12 and our additional test in the Appendix A. The red squares show the same signal measured using all 129 fields that passed H12 tests only. The error bars have been computed using the clone. Right-hand panel: display of the measured $\langle M_{\mathrm{ap}}^3(\theta) \rangle$ from the 120 *pass fields* together with the *WMAP*5 prediction and the average signal from the clone.

performed essentially from the same sample, therefore, the change in amplitude at aperture radii $\gtrsim 15$ arcmin may be indicative of residual PSF systematics on these scales. The right-hand panel of Fig. 4 shows the CFHTLenS measurement of $\langle M_{\mathrm{ap}}^3(\theta) \rangle$ for the *pass fields* in comparison to the predicted signal for a *WMAP*5 cosmology, and again the measurement from the clone.

In Fig. 5, we compare our measurement of the EEE mode to the other modes of $\langle M_{\mathrm{ap}}^3(\theta) \rangle$, and we possibly find more evidence for PSF systematics on scales of a few arcmin and below. For scales $\theta \gtrsim 3$ arcmin, the EEE signal is roughly one order of magnitude larger than the B- and parity modes whenever it is not consistent with zero. Meanwhile, the amplitudes of the B- and parity modes are for $\theta \lesssim 5$ arcmin clearly larger than those measured on the idealistic data in the clone, Fig. 2, where typical amplitudes are always smaller than $10^{-9}$. Possible origins of the increase of the systematics indicators can be IAs and PSF residuals, both of which are not accounted for in the clone. In principle, IA can generate B-modes, but the correlations in the source ellipticities should remain parity invariant. The presence of both parity modes EEB and BBB signals hence indicates that IA alone cannot explain the systematics in the data. This hints to an imperfect PSF correction in the shape measurement

that may be relevant for $\langle M_{\mathrm{ap}}^3 \rangle$. This further supports our decision to reject measurements below 5 arcmin in the cosmological analysis.

Nevertheless IA could also affect the measurement of our cosmological shear signal (Semboloni et al. 2008; Merkel & Schäfer 2014; Valageas 2014). For this reason, we try to quantify the impact of IA. Using *N*-body simulations, Semboloni et al. (2008) find that mostly the IA of early-type galaxies contaminates three-point shear statistics. In their model intrinsic ellipticities of galaxies are given by the ellipticity of the parent matter halo. Early-type galaxies are perfectly aligned to the halo, whereas spiral galaxies have a random misalignment to their parent halo. In surveys comparable to CFHTLenS wide, the IA amplitude of the EEE signal due to intrinsic–intrinsic–intrinsic (III) correlations becomes strong compared to the cosmic shear signal for aperture radii below a few arcmin and grows to a comparable amplitude at ∼1 arcmin. By considering tidal torque theory Merkel & Schäfer (2014) find that third-order correlations between the intrinsic shapes of sources and shear (GGI) are negligible with respect to the III correlations for our angular scales of interest; the absolute amplitude of III and GGI correlations is highly uncertain in their model though. Using the assumption of a linear relation between intrinsic shapes and
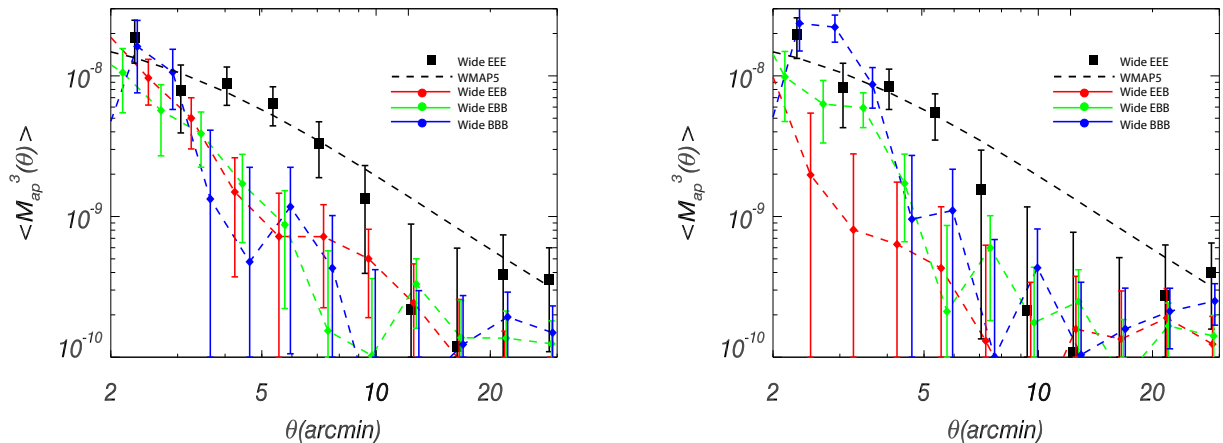


**Figure 5.** Left-hand panel: comparison of the CFHTLenS EEE mode of $\langle M_{\mathrm{ap}}^3(\theta) \rangle$ (black data points) to the absolute values of EEB, EBB, and BBB modes (red, green, and blue lines). The error bars have been computed using the clone. The dashed black line is a *WMAP*5 prediction. Right-hand panel: same quantities as in the left-hand panel after excluding elliptical galaxies, i.e. sources with BPZ $T_{\mathrm{B}} \leq 2$.

the local matter density as well as hierarchical clustering, Valageas (2014) finds that IA contamination is of the level of typically about 10 per cent for different source redshifts which is ubiquitous in our data. This figure includes a bias due to lens–source clustering which arises because of a correlation of source number density and the matter density (treated as linear in the model). In summary, these pieces of research imply that IA alignments should make only a small contribution to the total EEE signal for $\theta \gtrsim 5$ arcmin but may be substantial for $\theta \sim 1$ arcmin.

Using the conclusions from Semboloni et al. (2008), it is possible to evaluate the impact of III in our analysis by measuring the three-point signal with and without elliptical galaxies. The effective removal of ellipticals is achieved by selecting galaxies with classification $T_B > 2$ from the Bayesian photometric redshift estimation (BPZ; Benitez 2000; Heymans et al. 2013). This decreases the effective number of sources by about 20 per cent. With this selection the change in the EEE signal is within the error bars, as we show in the right-hand panel of Fig. 5. The EBB, EEB, and BBB components qualitatively retain their behaviour compared to the full galaxy sample: their amplitude is large at small aperture radii and falls off quickly. The amplitude itself, however, changes in a way that is difficult to reconcile with IA: the BBB signal increases significantly at about 3 arcmin rather than decreasing as anticipated. Our result therefore suggests that (i) the systematics are associated with residual PSF systematics which affect late-type galaxies more than early-type galaxies and (ii) that the precision of the measurement is still not sufficient to set constraints on the IA from the three-points statistics alone. For reason (i), we decide not to apply a morphological cut for our cosmological analysis. Hence our final catalogue is composed of 120 *pass fields* with the original selection cuts previously described in Section 2. The final selection of pointings correspond to a total effective area of roughly 100 deg², with masked regions taken into account.

Fig. 6 shows, for this final catalogue, the measurement of the *full* $\langle M_{\rm ap}^3(\theta_1, \theta_2, \theta_3) \rangle$ in comparison to the *WMAP*5 predictions and the clone measurement. As before with the equilateral $\langle M_{\rm ap}^3(\theta) \rangle$ we find a reasonable agreement also between the full statistics of the measurement, *WMAP*5 prediction, and the clone. For $\theta_i \lesssim 5$ arcmin, the SC01 model falls slightly below the clone, on larger scales the CFHTLenS measurement appears to be below the prediction; the statistical errors are, however, relatively large in this regime. In the next section, we use this vector of data points for $\theta_i \geq 5$ arcmin to infer cosmological parameters through a likelihood analysis.

### 4.3 Evidence for a non-Gaussian likelihood

The matter density field obeys non-Gaussian statistics for smoothing scales below the typical size of large galaxy clusters, and it asymptotically approaches Gaussian statistics towards larger scales and higher redshifts for a Gaussian primordial density field. Because of this non-Gaussian nature on small physical scales we expect that measurements of the three-point statistics of cosmic shear will exhibit a distinct non-Gaussian distribution on small angular scales, if these scales are not dominated by the shape noise of the sources. In order to investigate whether the estimator of $\langle M_{\rm ap}^3 \rangle$ shows any signs of non-Gaussianity, we study its distribution in 184 realizations of the `clone` for both the *noise-free* and the *noisy* samples. For this purpose, we compute estimates of $\langle M_{\rm ap}^3 \rangle$ for the same combination of aperture radii as for the CFHTLenS data. The resulting 184 simulated data vectors represent the likelihood of obtaining a value of $\langle M_{\rm ap}^3(\theta) \rangle$ on a 12.84 deg² survey (corresponding to the field of

view of each simulation), given the particular set of cosmological parameters in the clone.

The distributions are shown in Fig. 7, for angular scales $\theta = 3.4$, 30.0 arcmin of the equilateral $\langle M_{\rm ap}^3 \rangle$. The functional form of these distributions depends on the sampling and the presence of shape noise (*noisy*). In order to better illustrate the non-Gaussian feature of the likelihoods we plot their best-fitting Gaussian inside the panel; the Gaussian fits have the same mean and variance as our observed values. In this figure, we find clear deviations from a Gaussian model in the absence of shape noise, the observed distributions are skewed towards large values of $\langle M_{\rm ap}^3 \rangle$ (bottom panels). The skewness becomes weaker in the presence of shape noise but deviations from the Gaussian description are still discernible, especially for $\theta = 30$ arcmin (top right-hand panel).

For the range of angular scales considered in this paper, the non-Gaussian features are most prominent for $\theta \gtrsim 10$ arcmin as highlighted by Fig. 8. In this figure, we plot for Gaussian the average and for Quartiles the median of $\langle M_{\rm ap}^3(\theta) \rangle$ as function of $\theta$ using the simulations. In addition, we indicate as error bars the standard deviation times 0.67 (*Gaussian*) and the $\pm 25$ per cent quartiles (Quartiles). In the case of a Gaussian distribution of $\langle M_{\rm ap}^3 \rangle$, the data points and error bars of Gaussian and Quartiles should be identical, whereas differences indicate deviations from a Gaussian distribution for a given $\theta$. Such deviations become most obvious for $\theta \gtrsim 10$ arcmin, which could indicate that we have to find a non-Gaussian model of the likelihood for a cosmological analysis of CFHTLenS. To test this hypothesis in the following, we utilize the clone distribution of $\langle M_{\rm ap}^3 \rangle$ of the *noisy* sample to construct a numerically sampled non-Gaussian likelihood and compare its constraints on $(\Omega_{\rm m}, \sigma_8)$ to the constraints from a traditional analytical Gaussian model.

## 5 COSMOLOGICAL ANALYSIS

In this section, we describe the details of the cosmological analysis of $\langle M_{\rm ap}^3 \rangle$. For the analysis we use $N_{\rm d} = 20$ combinations of aperture radii in the range $5 \leq \theta_i \leq 30$ arcmin in $\langle M_{\rm ap}^3(\theta_1, \theta_2, \theta_3) \rangle$, shown in Fig. 6. We combine all $N_{\rm d}$ data points into one data vector $\boldsymbol{d}$. The key features of our analysis are a non-Gaussian likelihood function that we estimate from the clone and a data compression to suppress the numerical noise in the final result. We compare the results of this analysis to the results with a standard Gaussian likelihood. Moreover, our new approach allows us to factor in model uncertainties as well as measurement noise. We include errors due to shape noise, cosmic variance, measurement errors of source ellipticities, uncertainties in the Hubble parameter, and a multiplicative error in the overall amplitude of the predicted matter bispectrum. We embed everything into a Monte Carlo scheme for which no analytical form of the likelihood has to be specified; only realizations of statistical errors have to be provided.

### 5.1 Model parameters and priors

For the comparison of our non-Gaussian likelihood to a standard Gaussian likelihood, we jointly constrain the two cosmological parameters of a flat $\Lambda$CDM cosmology with a cosmological constant $\Omega_\Lambda = 1 - \Omega_{\rm m}$: the matter density $\Omega_{\rm m}$ and the rms dispersion $\sigma_8$ of matter fluctuations on a scale of $8\,h^{-1}$ Mpc linearly evolved to the Universe of today. Moreover, we assume for the Hubble parameter $H_0 = h\,100\,{\rm km\,s^{-1}}$ a Gaussian prior with mean $h = 0.7$ and relative variance of 5 per cent, compatible with the CMB-only constraints
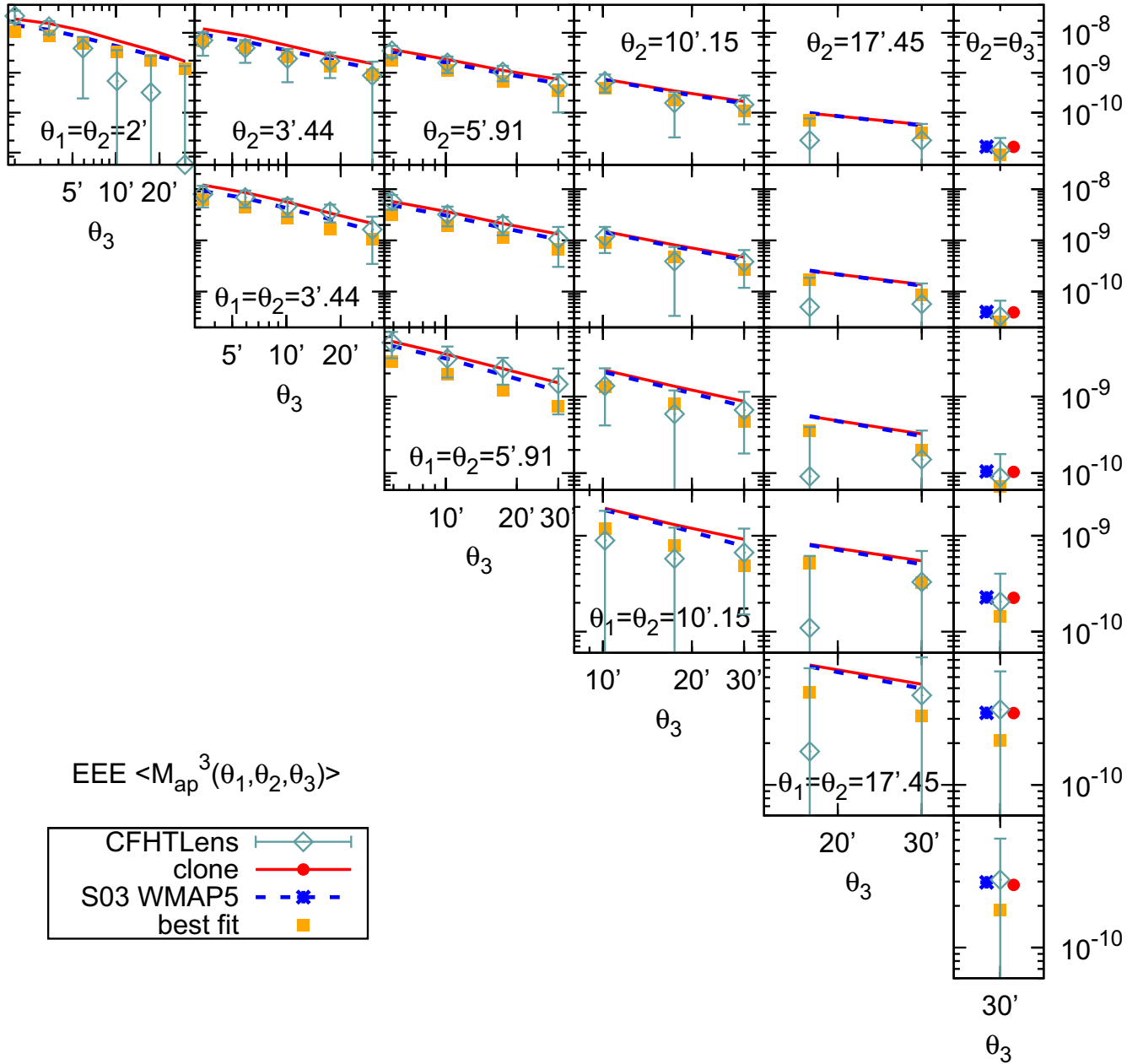
**Figure 6.** Measurements of the EEE $\langle M_{ap}^3(\theta_1, \theta_2, \theta_3)\rangle$ in the 120 CFHTLenS *pass fields* (dark green diamonds). The aperture radii $\theta_i$ are quoted in units of arcmin. The error bars have been computed using 184 sight lines of the clone. The average signal in the simulations is shown in red (solid lines or filled circles), and the analytical *WMAP*5 predictions with the SC01 bispectrum are shown in blue (dashed lines or stars). Each panel shows the EEE signal as a function of $\theta_3 \geq \theta_2$ for a fixed value of $\theta_1$ and $\theta_2$. Panels on the diagonal correspond to equilateral configurations with, increasing size from top to bottom. In each row, from left to right we increase the size of $\theta_2$, keeping $\theta_1$ fixed. The filled orange boxes are the best-fitting $(\Omega_m, \sigma_8) = (0.32, 0.7)$ of the SC01 model to the CFHTLenS data for $\theta_i \geq 5$ arcmin. For details see Section 6.

of *WMAP*5 for a flat universe. We compile the model parameters into the parameter vector $\boldsymbol{p} = (\Omega_m, \sigma_8, h)$. All other cosmological parameters are fixed to their *WMAP*5 best-fitting values to be consistent with the clone; see Sections 3.1 and 3.2 for all relevant model parameters. We denote all priors by the PDF $P_p(\boldsymbol{p})$.

In addition, we assume that the overall amplitude of $\langle M_{ap}^3 \rangle$ can only be predicted up to multiplicative factor $1 + f$ with a Gaussian prior $P_f(f)$ of rms 20 per cent and mean $\langle f \rangle = 0$. This directly accounts for the spread in predictions for the matter bispectrum by competing models (see Fig. 3).

### 5.2 Likelihood

Let $\boldsymbol{d}$ be a vector of observables in an experiment, such as our measurements of $\langle M_{ap}^3 \rangle$. For the statistical analysis of these data $\boldsymbol{d}$, we can distinguish between two categories of errors.

First, errors originating from the theory side, or *theory errors*, which depend on the model parameters $\boldsymbol{p}$ in general. Theory errors are present if a model $\boldsymbol{m}(\boldsymbol{p})$ cannot perfectly fit $\boldsymbol{d}$ in the total absence of measurement noise. In our analysis, three kinds of theory error are accounted for: cosmic variance, intrinsic shapes of the sources, and model uncertainties in the (cosmic average) matter bispectrum.
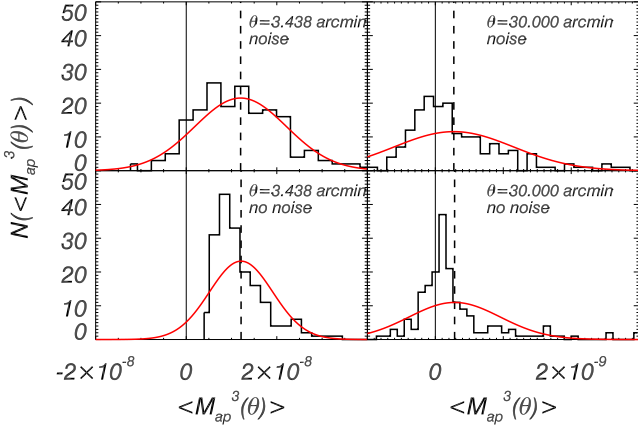
**Figure 7.** Top panels: frequency of values of the equilateral $\langle M_{\mathrm{ap}}^3(\theta)\rangle$ from 184 lines-of-sight from *noisy* version of the clone (12.84 deg²). In the left-hand panels, we show the result for $\theta = 3.438$ arcmin, while in the right-hand panels we show the distribution for $\theta = 30$ arcmin. Black dashed lines show the average values, while the solid red lines indicate the best-fitting Gaussian. The black solid line indicates the zero value. Bottom panel: the same as the top panels but for the *noise-free* version of the clone.
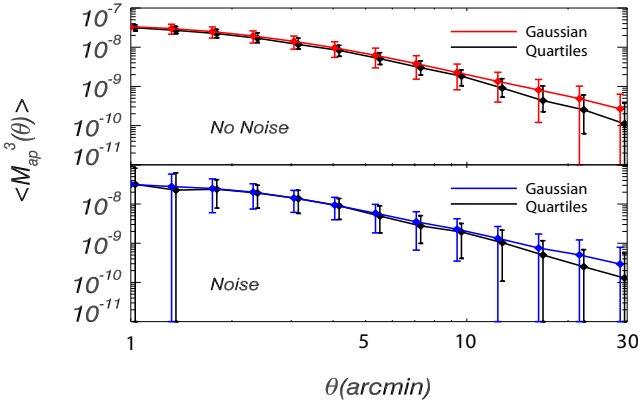


**Figure 8.** Top panel: median signal and the ±25 per cent quartiles obtained from the 184 *noise-free* clone realizations (black line; Quartiles). We compare this signal with the average signal and its error which is obtained multiplying the standard deviation by 0.67 (red line; Gaussian). In the case of a Gaussian distribution, the curves should coincide and the error bars should be the same. Bottom panel: same results as top panel but using the *noisy* version of the clone.

Cosmic variance arises because our model predicts the cosmic average of $\langle M_{\mathrm{ap}}^3\rangle$ but not the statistics for a particular volume of the Universe. Intrinsic shapes of sources are not observable although they can practically be inferred with reasonable assumptions. Hence intrinsic galaxy shapes are nuisance parameters in our model that we marginalize over. And, as reflected by Fig. 3, there is a set of theoretical models for the matter bispectrum currently available that vary among themselves by about 20 per cent in amplitude for the range of angular scales that we study here. We parametrize this particular theory uncertainty by the nuisance parameter $f$.

Secondly, even if a model fits the data we expect residuals of the fit due to errors in the measurement process: the *measurement noise*. Measurement noise is by definition only related to the observables and hence unrelated to $p$. Our main source of measurement errors, and the only one we account for here, are uncertainties in the galaxy ellipticities $\epsilon_i$. Other conceivable sources such as source positions or their redshifts are neglected here.

In our model of $d$, we include theory and measurement errors by the ansatz:

$$d = (1 + f)m(p) + \Delta d(p) =: m_f(p) + \Delta d(p), \tag{39}$$

where $f$ is the multiplicative error in the model amplitude $m(p)$, while $\Delta d(p)$ comprises all remaining theory and measurement errors combined. In more complex applications, theory errors and measurement errors could be separated and simulated independently from each other. On average we have $\langle \Delta d(p)\rangle = 0$ and $\langle f\rangle = 0$. Our model of the likelihood function is then as follows. We denote by $P_{\Delta d}(\Delta d|p)$ the probability density of an error $\Delta d$ given the parameters $p$. To include the error of $f$, we then write the likelihood $\mathcal{L}(d|p)$ of $d$ given $p$ as

$$\mathcal{L}(d|p) = \int \mathrm{d}f\, P_f(f)P_{\Delta d}\left(d - m_f(p)|p\right). \tag{40}$$

Up to a normalization constant $E(d)$ the posterior PDF of $(\Omega_{\mathrm{m}}, \sigma_8)$ given $d$ is therefore

$$P_p(\Omega_{\mathrm{m}}, \sigma_8|d) = E^{-1}(d) \int \mathrm{d}h\, P_p(p)\mathcal{L}(d|p). \tag{41}$$

The exact value of the so-called evidence $E(d)$ is irrelevant for this analysis and hence set to unity. The Hubble parameter $h$ is weakly constrained by the data. Therefore, we marginalize the posterior over $h$.

A reasonable and common approximation of the likelihood $\mathcal{L}(d|p)$ would be a multivariate Gaussian PDF as, for instance, applied in F14. As shown in Section 4.3 by our simulation of the CFHTLenS data set, however, the $\langle M_{\mathrm{ap}}^3\rangle$ measurement exhibits deviations from Gaussian statistics. This motivates us to apply a non-Gaussian model of the likelihood. Towards this goal, we outline in the following an algorithm that estimates $\mathcal{L}(d|p)$ based on a discrete set of Monte Carlo realizations of $\Delta d(p)$ for the posterior $P_p(\Omega_{\mathrm{m}}, \sigma_8|d)$.

### 5.3 Monte Carlo sampling of likelihood

An opportunity for an approximation of $\mathcal{L}(d|p)$ by a Monte Carlo process can be seen by rewriting the PDF $P_{\Delta d}$ as

$$P_{\Delta d}(\Delta d|p) = \int \mathrm{d}\Delta x\, P_{\Delta d}(\Delta x|p)\delta_{\mathrm{D}}\left(\Delta d - \Delta x\right) \tag{42}$$

$$\approx \frac{1}{N_{\Delta d}} \sum_{k=1}^{N_{\Delta d}} \delta_{\mathrm{D}}\left(\Delta d - \Delta x_k\right), \tag{43}$$

with $\delta_{\mathrm{D}}(x)$ being the Dirac delta function. The sum in last line approximates the integral in the first line by a numerical Monte Carlo integration with $N_{\Delta d}$ points $\Delta x_k$ (Press, Teukolsky & Vetterling 1992). For this approximation, we produce, for a given $p$, $N_{\Delta d}$ random realizations of $\Delta x$ from $P_{\Delta d}(\Delta x|p)$ by means of the clone. We denote this process simply by $\Delta x_k \curvearrowleft P_{\Delta d}(\Delta x|p)$ in the following. In the limit $N_{\Delta d} \to \infty$, the number density of the points $\Delta x_k$ at $\Delta d$ converges to $P_{\Delta d}(\Delta d|p)$ up to a normalization constant. Even for finite $N_{\Delta d}$, the number density of points still provides a useful estimator for the likelihood. This is the basis of our Monte Carlo scheme. For this scheme, we address the infinite noise in the previous estimator by smoothing the number density of sampling points.

## 5.4 ICA-based interpolation

Let $\Delta x_k \frown P_{\Delta d}(\Delta x | p)$ be a sample of $N_{\Delta d}$ simulated discrete points with average $\langle \Delta x_k \rangle = 0$. In addition, let the matrix $\mathsf{N} = \sum_k \Delta x_k \Delta x_k^{\mathrm{T}} / N_{\Delta d}$ be an estimator of the covariance of $\Delta x_k$. Our aim is to use the smoothed local number density of the set of points $\{\Delta x_k\}$ at $\Delta d$ as approximation of $P_{\Delta d}(\Delta d | p)$. To this end, we exploit the independent component analysis (ICA) to factorize the sparsely sampled higher dimensional likelihood $P_{\Delta d}(\Delta d | p)$ into a product of 1D histograms as in Hartlap et al. (2009). We refer the reader to this paper for a general discussion of the ICA and only briefly summarize the practical steps here.

The ICA defines a linear transformation $\mathsf{M}$ and new coordinates $c := \mathsf{M}\mathsf{N}^{-1/2}\Delta d$ that allow us to express the $N_{\mathrm{d}}$-dimensional PDF,

$$P_{\Delta d}(\Delta d | p) \approx \det \mathsf{M}\mathsf{N}^{-1/2} \times \prod_{i=1}^{N_{\mathrm{d}}} P_c^{(i)}\left([\mathsf{M}\mathsf{N}^{-1/2}\Delta d]_i \,\middle|\, p\right), \quad (44)$$

as a product of the 1D probability densities $P_c^{(i)}(c_i | p)$. The constant pre-factor on the right-hand side is the Jacobian of the mapping $\mathsf{M}\mathsf{N}^{-1/2}$. Therefore, by means of the ICA all components $c_i$ of $c$ are made statistically independent. Note that for a Gaussian $P_{\Delta d}(\Delta d | p)$ the ICA is essentially a principal component analysis. We estimate the transformation matrix $\mathsf{M}$ from $\{\Delta x_k\}$ by application of the FASTICA algorithm (Hyvarinen 1999). The matrix $\mathsf{M}$ is a $N_{\mathrm{d}} \times N_{\mathrm{d}}$ square matrix in our case, i.e. the number of components of $c$ and $\Delta d$ are the same.

For the sample $\{\Delta x_k\}$, the ICA transformation then gives us a new set of $N_{\Delta d}$ sampling points $c_k := \mathsf{M}\mathsf{N}^{-1/2}\Delta x_k$. We denote the $i$-components of $c_k$ by $c_{ki} = [c_k]_i$. For a fixed $i$, we adaptively smooth the 1D frequency distribution of these points $\{c_{ki}\}$ to produce the histogram $Q_{\mathrm{ica}}^{(i)}(x; c_{ki})$ and use its value at $x = c_i$ as an estimator of $P_c^{(i)}(c_i | p)$. Specifically, to obtain $Q_{\mathrm{ica}}^{(i)}(x; c_{ki})$ we apply a 10th neighbour adaptive smoothing: for a given value $x$ we find the distance $d_{10,i}(x) := |x - c_{10,i}|$ to the 10th nearest neighbour sampling point $c_{10,i} \in \{c_{ki}\}$ for fixed $i$ and then compute

$$Q_{\mathrm{ica}}^{(i)}(x; c_{ki}) = \frac{10}{d_{10,i}(x)}. \quad (45)$$

In doing so, we bin for every index $i$ the 1D distribution of values $\{c_{ki}\}$ with an adaptive bin width $d_{10,i}(x)$ that depends on the local density of the points $\{c_{ki}\}$ at $x$ (Loftsgaarden & Quesenberry 1965). We find that this technique is more robust compared to the Gaussian kernel method with fixed kernel size in Hartlap et al. (2009), if the PDF sampling has a few extreme outliers in the tail of the distribution.

Finally, our approximation of the logarithm of $P_{\Delta d}(\Delta d | p)$ is given by

$$\ln P_{\Delta d}(\Delta d | p) \approx \ln Q_{\mathrm{ica}}(\Delta d; \Delta x_k)$$
$$:= \eta + \sum_{i=1}^{N_{\mathrm{d}}} \ln Q_{\mathrm{ica}}^{(i)}\left([\mathsf{M}\mathsf{N}^{-1/2}\Delta d]_i; c_{ki}\right), \quad (46)$$

where $\mathrm{e}^\eta$ is the normalization of $Q_{\mathrm{ica}}(\Delta d; \Delta x_k)$. The normalization $\eta$ can be ignored in our case because for this study it is identical for every position in the parameter space.

## 5.5 Data compression

The ICA interpolation technique is prone to a bias that underestimates the size of the credible intervals of the model parameters (Hartlap et al. 2009). This bias is large if $N_{\mathrm{d}}/N_{\Delta d} \sim 1$ and small for $N_{\mathrm{d}}/N_{\Delta d} \ll 1$; here $N_{\Delta d} = 200$ is our number of sampling points

of the likelihood and $N_{\mathrm{d}} = 20$ is the size of the uncompressed data vector. A similar problem affects traditional Gaussian likelihood analyses when the inverse covariance has been estimated from simulations (Hartlap, Simon & Schneider 2007; Taylor, Joachimi & Kitching 2013). In order to reduce this bias, we compress the size $N_{\mathrm{d}}$ of the data vector $d$, and we apply the same compression to the realizations $\Delta x_k$ in the ICA interpolation. This data compression also has the benefit to produce a smoother posterior of $p$ as the sampling noise in the interpolated likelihood is reduced.

Our data compression is based on a Karhunen–Loève (KL) transform (Tegmark, Taylor & Heavens 1997; Kilbinger & Munshi 2006; Asgari & Schneider 2014). It identifies $N_{\mathrm{d}}$ S/N modes of $d$ and rejects modes with a low S/N. This procedure allows us to find a linear projection $d' = \mathsf{C}d$ that reduces the number of elements of $d$ to $N_{\mathrm{d'}} < N_{\mathrm{d}}$. The projection matrix $\mathsf{C}$ is chosen such that most of the cosmological information on $p$ is still available in $d'$. Importantly, the KL transform – or any projection matrix $\mathsf{C}$ for that matter – at most decreases the constraints on $p$ but does not bias the result provided the data can be fit by the model. The KL transform affects the cosmological analysis and the ICA decomposition only in that far that we now use as data vector $d'$ instead of $d$, the compressed model vector $m'(p) = \mathsf{C}m(p)$, and the Monte Carlo realizations $\Delta x'_k = \mathsf{C}\Delta x_k$.

For a data compression matrix $\mathsf{C}$, we would like to identify linear combinations of the components of $d$ that vary strongly when changing the parameters $p$ (signal variance). On the other hand, in the presence of measurement noise and theory errors, we would also like to identify combinations that are most significant compared to noise. The KL transform finds a compromise of both. This means the KL transform identifies modes $e_i$ in $d$-space that have large ratios of signal variance and noise variance. The compression matrix $\mathsf{C} = (e_1, \ldots, e_{N_{\mathrm{d'}}})^{\mathrm{T}}$ comprises the $N_{\mathrm{d'}}$ KL modes with the highest S/N. To construct $\mathsf{C}$, we proceed in two steps.

First, we compute the signal covariance $\mathsf{S}$ of model vectors $m(p)$ over a volume $V$ in parameter space that is defined by our prior information $P_p(p)$ on the cosmological parameters:

$$\mathsf{S} = \int \frac{\mathrm{d}\Omega_{\mathrm{m}}\,\mathrm{d}\sigma_8\,\mathrm{d}h\,P_p(p)}{V}\,(m(p) - \langle m \rangle)(m(p) - \langle m \rangle)^{\mathrm{T}}, \quad (47)$$

where $V = \int \mathrm{d}\Omega_{\mathrm{m}}\,\mathrm{d}\sigma_8\,\mathrm{d}h\,P_p(p)$, and

$$\langle m \rangle = \int \frac{\mathrm{d}\Omega_{\mathrm{m}}\,\mathrm{d}\sigma_8\,\mathrm{d}h\,P_p(p)}{V}\,m(p) \quad (48)$$

is the mean of $m(p)$. For the computation of $\mathsf{S}$ by integration, we adopt a flat prior $P_p(p)$ for $\Omega_{\mathrm{m}} \in [0.1, 1.0]$, $\sigma_8 \in [0.4, 1.0]$, and $h \in [0.6, 0.8]$. The previous integrals could in principle be estimated by a Monte Carlo process for which we (i) randomly and repeatedly draw parameters $p$ from the prior $P_p(p)$, (ii) compute $m(p)$, and (iii) determine the mean $\langle m \rangle$ and covariance $\mathsf{S}$ of all realizations of $m(p)$. The eigenvectors of $\mathsf{S}$ with the largest eigenvalue determine modes of $d$ that are most sensitive with regard to $p$.

Second, we compute the noise covariance, which is simply the covariance matrix $\mathsf{N}$ of $\Delta x$ for a chosen fiducial cosmology (Section 5.4). The data compression is thus optimal for the fiducial model. The KL modes are then the eigenvectors $e_i$ of the generalized eigenproblem:

$$\mathsf{S}e_i = \lambda_i \mathsf{N}e_i, \quad (49)$$

where $\lambda_i$ are the eigenvalues of $e_i$; the S/N of the mode $e_i$ is $\sqrt{\lambda_i}$.

In the top panel of Fig. 9, we show simulated data $\langle M_{\mathrm{ap}}^3 \rangle$ for our $N_{\mathrm{d}} = 20$ combinations of aperture radii (red bars). The KL modes are linear combinations of the aperture radii with relative weights
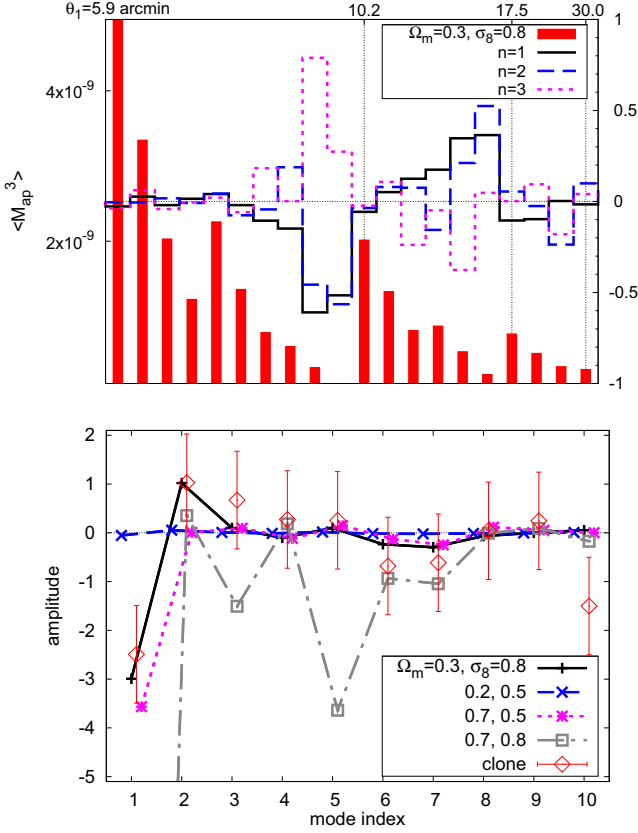
**Figure 9.** Illustration of the KL data compression. All models assume $h = 0.7$. Top panel: the red sticks show simulated data $\langle M_{\rm ap}^3 \rangle$ with $N_{\rm d} = 20$ elements sorted by increasing $\theta_1 \leq \theta_2 \leq \theta_3$; $\theta_i = 5.9, 10.2, 17.5, 30.0$ arcmin. The KL modes are averages of all data points with relative weights as indicated by the lines for the mode indices $n = 1, 2, 3$ (right-hand $y$-axis). Bottom panel: amplitudes of KL modes as function of the mode index for four different noise-free model vectors (lines); the open square data point at $n = 1$ is off the chart at an amplitude of approximately $-30$. The open diamonds show a one noisy clone data vector in comparison.

defined by the components of $e_i$. These weights are displayed as lines for the first three modes (right-hand $y$-axis). Importantly, the weights can have positive and negative signs. The lines show that our KL modes are mostly sensitive to large aperture scale radii with $\theta_i \geq 10.2$ arcmin. The bottom panel shows as lines four compressed model vectors $\mathbf{C}m(p)$ that do not contain noise in comparison to one noisy clone data vector. The error bars reflect the $1\sigma$ uncertainty for noise as in our CFHTLenS data. Except for models with large values of $\Omega_{\rm m}$ and $\sigma_8$ (grey dashed–dotted line) all models are essentially zero for KL mode indices larger than 3. This means their cosmological information is mostly inside the first couple of modes. Note that errors between different KL modes are uncorrelated and of equal variance by construction, i.e. $\langle \Delta d_i' \Delta d_j' \rangle = \delta_{ij}^{\rm K}$. Nevertheless, in the case of a non-Gaussian statistics, there may be higher order correlations such as $\langle \Delta d_i' \Delta d_j' \Delta d_k' \rangle \neq 0$ present in the data.

## 5.6 Bias correction

After a data compression with $N_{\rm d'} \leq 10$ and the following correction of the likelihood, we expect the bias in the size of the credible intervals of our sampled posterior to be negligible for the following reason. Hartlap et al. (2009) report that this bias is similar to the one known for a Gaussian likelihood for which the data covariance

is estimated from realizations of the data. In the Gaussian case, to de-bias the likelihood the inverse of the estimated covariance has to be rescaled by a factor $f_{\rm corr} = (N_{\Delta d} - N_{\rm d'} - 2)/(N_{\Delta d} - 1)$ or, equivalently, $\mathcal{L} \mapsto \mathcal{L}^{f_{\rm corr}}$. We apply the latter correction to our sampled likelihood $Q_{\rm ica}(\Delta d'; \Delta x_k')$ in equation (46). However, this correction is small since $f_{\rm corr} \geq 0.94$ for $N_{\rm d'} \leq 10$.

### 5.7 Sampling algorithm of posterior

We compute the posterior $P_p(\Omega_{\rm m}, \sigma_8 | d)$ on a $100 \times 100$ grid that covers the $(\Omega_{\rm m}, \sigma_8)$ plane. To compute the posterior value for a grid pixel we proceed in four steps.

(i) Generation of a set of $N_{\Delta d}$ realizations $d_k$ to sample the error $P_{\Delta d}(\Delta d | p)$ for a given $p$: We obtain the $d_k$ by measuring $\langle M_{\rm ap}^3 \rangle$ on the *noisy sample* of the clone, hence both the intrinsic galaxy shapes and the cosmic variance are simulated. In the simulation, the 1D variance of intrinsic source ellipticities is set to $\sigma_\epsilon = 0.28$ to account for both the true intrinsic variance and the measurement error of ellipticities; both are assumed to be Gaussian. From the clone patches, we compute a simulated $\langle M_{\rm ap}^3 \rangle$ for an effective CFHTLenS area of roughly $100\,{\rm deg}^2$ by combining the clone measurements of seven randomly selected sight lines. Each clone line-of-sight, out of 184 in total, covers $12.84\,{\rm deg}^2$. Repeating this procedure $N_{\Delta d} = 200$ times gives us the sample $\Delta x_k = d_k - \bar{d}$, where $\bar{d}$ expresses the average of all realizations $d_k$.

(ii) Determination of the data compression matrix $\mathbf{C}$ for a given covariance $\mathbf{N}$ of $\{\Delta x_k\}$, models $m(p)$, and the model prior $P_p(p)$: see Section 5.5 for details. From this we compute the compressed vectors $d' = \mathbf{C}d$ and $\Delta x_k' = \mathbf{C}\Delta x_k$. We compute the compression matrix $\mathbf{C}$ once for a fiducial cosmology and use it for all $p$.

(iii) ICA factorization of the compressed $P_{\Delta d'}(\Delta d' | p)$ into a product of interpolated, 1D histograms $Q_{\rm ica}^{(i)}(x; c_{ki})$ by means of an ICA of the sample $c_{ki} = [\Delta x_k']_i$: see Section 5.4 for details.

(iv) Marginalization over the multiplicative factor $f$ and the Hubble parameter $h$ to obtain the posterior value $P_p(\Omega_{\rm m}, \sigma_8 | d')$: we perform the marginalization by another Monte Carlo integration that draws $N_{\rm fh} = 500$ values $f_i \frown P_f(f)$ and the same amount of values $h_i \frown N(0.7, \sigma_h)$ from a Gaussian prior for the Hubble parameter. With these values we compute

$$P_p(\Omega_{\rm m}, \sigma_8 | d') \approx \frac{1}{N_{\rm fh}} \sum_{i=1}^{N_{\rm fh}} \left[ Q_{\rm ica}(d' - m_{{\rm f},i}'(p_i); \Delta x_k') \right]^{f_{\rm corr}}, \quad (50)$$

where $m_{{\rm f},i}'(p_i) = m'(p_i)(1 + 0.2 f_i)$ is the rescaled model $m'(p_i)$ for $p_i = (\Omega_{\rm m}, \sigma_8, h_i)$. The approximation $Q_{\rm ica}(\Delta d'; \Delta x_k')$ depends on the factors $Q_{\rm ica}^{(i)}(x; c_{ki})$, see equation (46).

Ideally, step (i) is repeated for any new value of $p$ based on a simulation for a fiducial cosmology with parameters $p$. To keep the simulation effort viable, however, we assume that the scatter of $d_k$ is as in the clone for any $p$ in the entire parameter space explored. Therefore step (i) only has to be performed once. For a Gaussian likelihood, this assumption would be equivalent to using the same likelihood covariance for all $p$, which is indeed a common assumption as e.g. in F14 (for a discussion see Eifler, Schneider & Hartlap 2009; Kilbinger et al. 2013). In a future application of our technique, subject to less prohibitive computational constraints, a computation of the sampled likelihood for different $p$ is conceivable.

Finally, it is likely that we moderately underestimate the scatter of $\Delta x_k$ in step (i) due to cosmic variance. The 184 realizations of the clone allow only for 26 independent realizations of a $100\,{\rm deg}^2$ survey; the cosmic variance between the $\Delta x_k$ is partially correlated.

## 5.8 Tests of the posterior construction

In this section, we test the robustness and accuracy of our code implementation of Section 5.7 before its application to the CFHTLenS data.

We start by looking at different degrees of data compression in the top panel of Fig. 10. For this purpose, we use a noise-free model vector $\boldsymbol{m}(\boldsymbol{p})$ with the parameters $\boldsymbol{p} = (\Omega_{\mathrm{m}}, \sigma_8, h) = (0.3, 0.8, 0.7)$ as input to the cosmological analysis. We plot three credible regions of the resulting posterior $P_p(\Omega_{\mathrm{m}}, \sigma_8 | \boldsymbol{d})$. The maximum of all posteriors coincides with the parameters of the input vector (not shown). The figure supports our earlier expectation that only few KL modes are required for the analysis: there is no clear improvement for $N_{d'} \geq 3$. The differences between the panels are likely due to numerical noise in the sampled likelihood for the following reason. In Fig. 10 we plot the posterior of the combined quantity $\Sigma_8 = \sigma_8 (\Omega_{\mathrm{m}}/0.27)^{0.64}$ for the previous model data vector but devising now a Gaussian likelihood. This likelihood model is not subject to sampling noise as its analytical form is completely determined. As can be seen, the posterior $P_p(\Sigma_8 | \boldsymbol{d'})$ is virtually unchanged for $N_{d'} \geq 3$. Therefore, the first two modes contain all cosmological information of the model data. The same is presumably true for the non-Gaussian case so that all variation in the top panel can be attributed to numerical noise.

As can be seen in Fig. 9 (unlikely) models with values high in both $\Omega_{\mathrm{m}}$ and $\sigma_8$ exhibit some signal until the mode $n = 7$. Therefore, we set $N_{d'} = 5$ in our final CFHTLenS analysis as compromise between sampling noise and cosmological information. Moreover, the middle panel shows that the inclusion of a 20 per cent systematic error in the model amplitude has a small impact on the posterior information (solid black line). It slightly stretches the uncertainty towards larger values of $\Sigma_8$.

For the bottom panel of Fig. 10, we test the accuracy of our analytical matter bispectrum and that of the likelihood analysis by means of the clone. We run our analysis code for 26 independent simulated CFHTLenS-like data vectors created using *noise-free* realizations; we combine the 184 patches into 26 groups of seven data vectors. The figure shows three credible regions of the combined posterior of all 26 analyses. We attain the combined posterior by adding the 26 individual logarithmic posteriors on a grid. Ideally, the resulting posterior should be consistent with the cosmological parameters in the clone that we indicate by the intersection of the two dashed lines. The contours, however, indicate with about $3\sigma$ a model bias due to which we do not perfectly recover the clone cosmology: the centre of the contours, indicated by the black point, is offset in $\sigma_8$ by a few per cent and in $\Omega_{\mathrm{m}}$ by roughly 10 per cent. However, this offset is still small compared to the CFHTLenS noise levels, which can be seen by comparing offset in the bottom panel to the size of the credible regions in the top panel. To assure that the bias is unrelated to either the data compression or the ICA interpolation of the likelihood, we also determine the maximum of the posterior for the average, uncompressed clone data vector for a simple Gaussian likelihood. We find biased values consistent with the non-Gaussian results of compressed data. Our interpretation is that the bias originates from a small mismatch between the analytic model and the clone average that is still visible at 5 arcmin (EEE mode in Fig. 2).

In conclusion, there is a systematic bias in our analytic model for the third-order aperture statistics as revealed by our comparison to $N$-body simulated data. Since this bias is small relative to the levels of shape noise and cosmic variance in CFHTLenS we can ignore it for the scope of this paper. For the analysis of next generation
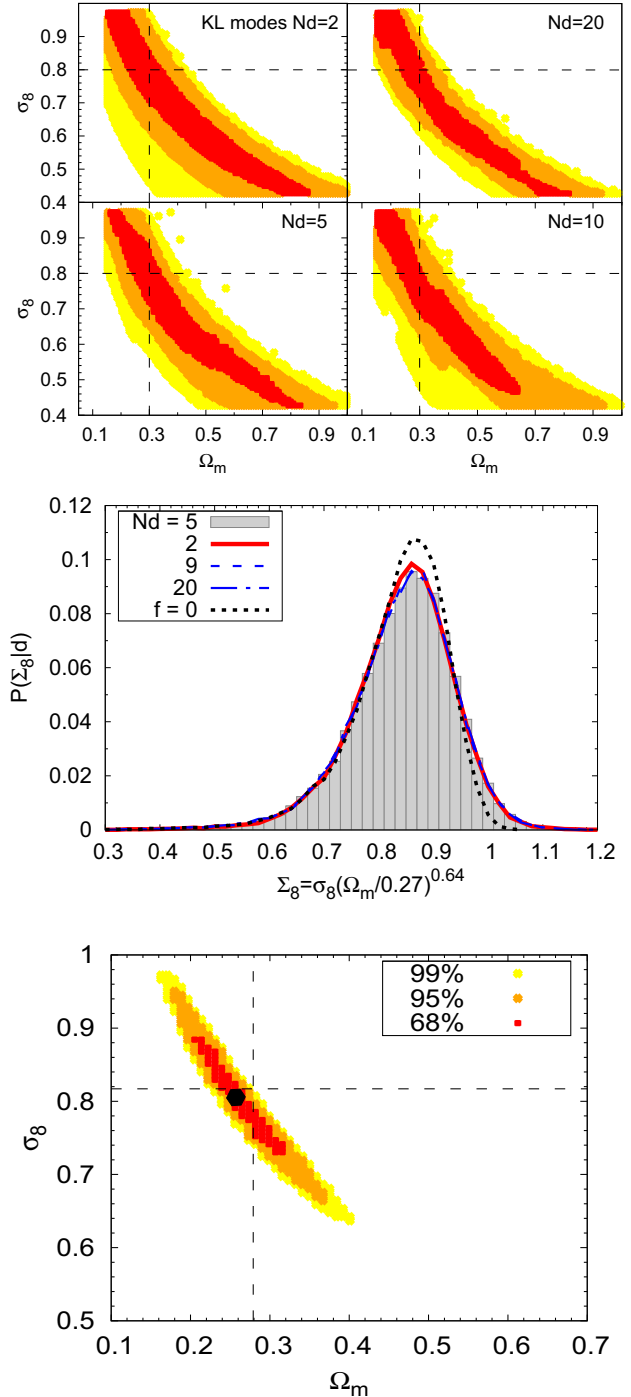


**Figure 10.** Results of our code tests running on mock data. Top panel: a series of cosmological analyses using different degrees of data compression. All four runs use same simulated data vector with $\Omega_{\mathrm{m}} = 0.3$, $\sigma_8 = 0.8$, and $h = 0.7$ but a different number of KL modes as indicated. The coloured regions highlight the 68, 95, and 99 per cent credible regions for a flat cosmology. Insets with more KL modes $N_{d'}$ are subject to more numerical noise. Middle panel: the posterior of $\Sigma_8 = \sigma_8 (\Omega_{\mathrm{m}}/0.27)^{0.64}$ for the test data vector for different degrees of compression and a Gaussian likelihood. The dotted black solid line uses $N_{d'} = 5$ and no error in the model amplitude ($f = 0$). Bottom panel: results of a verification run of the analysis code. The credible regions reflect the combined constraints from 26 simulated *noise-free* CFHTLenS measurements in the clone simulation. The posterior is offset with respect to the fiducial model ($\Omega_{\mathrm{m}} = 0.279$, $\sigma_8 = 0.817$; dashed black lines).

surveys, on the other hand, more accurate models of $\langle M_{\mathrm{ap}}^3 \rangle$ will be needed.

## 6 RESULTS

We present our constraints of $\sigma_8$ and $\Omega_{\mathrm{m}}$ for the CFHTLenS data for a flat $\Lambda$CDM model in Fig. 11. Therein we include only measurements of the EEE mode of $\langle M_{\mathrm{ap}}^3(\theta_1, \theta_2, \theta_3) \rangle$ for $\theta_i = 5.9, 10.2, 17.5, 30.0$ arcmin. In order to avoid confirmation bias in the generation of this result, we blindly analysed four data sets simultaneously of which three were noisy mock data and one was the CFHTLenS data vector with the results shown here. The CFHTLenS data vector was revealed only after the cosmological analysis. Furthermore, we
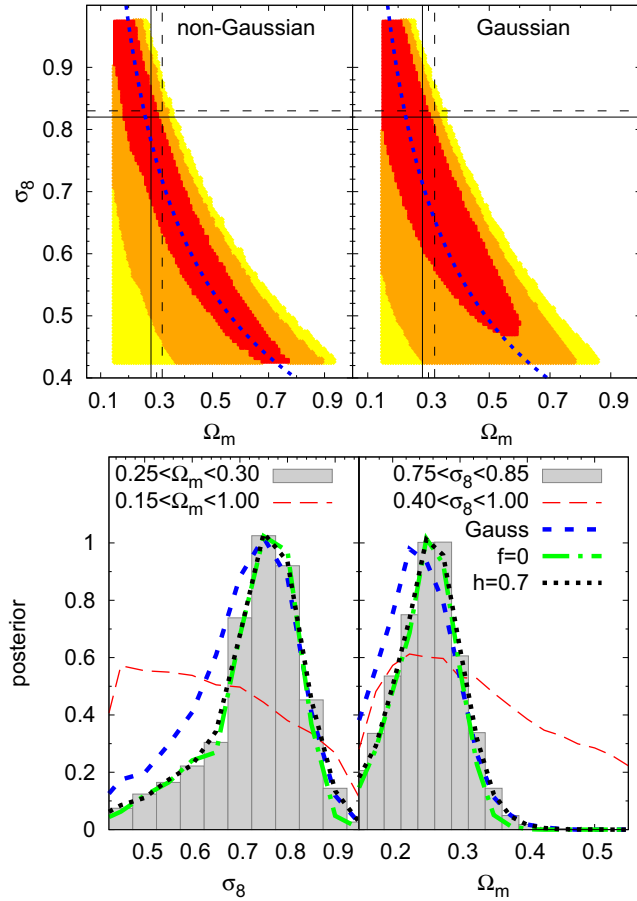


**Figure 11.** Top panel: constraints in the $\sigma_8$–$\Omega_{\mathrm{m}}$ plane from the CFHTLenS $\langle M_{\mathrm{ap}}^3 \rangle$ for a flat $\Lambda$CDM cosmology with 5 per cent uncertainty on $h = 0.7$ and a 20 per cent uncertainty in the model amplitude (credibility red: 68 per cent; orange: 95 per cent; yellow: 99 per cent). The dashed lines indicate the *Planck* best-fitting parameters, the solid lines *WMAP*9 parameters. The left-hand inset depicts the posterior for a non-Gaussian likelihood, whereas the right-hand inset is based on a Gaussian model. The dotted line on the left (right) corresponds to the best-fitting value of $\Sigma_8 = \sigma_8(\Omega_{\mathrm{m}}/0.27)^{0.64} = 0.8(0.73)$. Bottom panel: marginalized cosmological results for $\sigma_8$ (left) and $\Omega_{\mathrm{m}}$ (right) alone with different top-hat priors on the parameters (as indicated). The thick blue dashed line indicates constraints from the Gaussian likelihood in comparison to the non-Gaussian likelihood (grey area). The thick dotted black line is non-Gaussian constraints for a fixed $h = 0.7$, whereas the thick dotted–dashed green lines $f = 0$ do not include the 20 per cent multiplicative error in the model amplitude. Except for the red dashed lines, the posteriors are normalized to their value at the maximum.

performed the analysis after the systematics checks of the data and after our final decision on the usable range of angular scales. In particular, we did not use the CFHTLenS data during the development and testing phase of the analysis code in any way (Section 5).

In the top panel of Fig. 11, we show the 68, 95, and 99 per cent credible regions for the joint constraints of the matter density parameter $\Omega_{\mathrm{m}}$ and the amplitude $\sigma_8$ of the matter density fluctuations. We performed the analysis twice: once with the non-Gaussian model of the likelihood for the left-hand inset (non-Gaussian), and once with a Gaussian likelihood for the right-hand inset (Gaussian). The Gaussian likelihood is based on the noise covariance matrix **N** in Section 5.4. Both posteriors use the same degree of data compression (five KL modes). For reference we have indicated the slightly differing best-fitting values of *WMAP*9 and *Planck* as solid and dashed lines, respectively (Hinshaw et al. 2013; Planck Collaboration XVI 2014). In summary, there is little difference in the posteriors, mostly visible between the 68 per cent credible regions. Both constraints are highly degenerate and basically only exclude simultaneously large values of $\Omega_{\mathrm{m}}$ and $\sigma_8$.

In order to break the degeneracy of the parameters for the bottom panel of Fig. 11, we assume an additional prior on either $\Omega_{\mathrm{m}}$ (left) or $\sigma_8$ (right). The top-hat priors are centred around $\Omega_{\mathrm{m}} = 0.275$ and $\sigma_8 = 0.8$, close to the best-fitting values of the *WMAP*9 results. The widths of the top-hats are $\Delta\Omega_{\mathrm{m}} = 0.05$ and $\Delta\sigma_8 = 0.1$. The resulting marginalized posteriors of the non-Gaussian data model are shown as grey bars. With these strong priors we infer $\Omega_{\mathrm{m}} = 0.27^{+0.05}_{-0.05}$ and $\sigma_8 = 0.77^{+0.07}_{-0.11}$ (68 per cent credibility). Furthermore, without the imposed top-hat priors the marginalized posterior of either parameter yields only weak constraints (thin dashed red lines), which are essentially just the upper limits $\Omega_{\mathrm{m}} \leq 0.45(0.67)$ and $\sigma_8 \leq 0.75(0.93)$ for a 68 per cent (95 per cent) credibility. These upper limits depend on the adopted broad priors of $0.15 \leq \Omega_{\mathrm{m}} \leq 1$ and $0.4 \leq \sigma_8 \leq 1$ due to the strong degeneracy of both parameters. Therefore, it is more relevant to combine $(\Omega_{\mathrm{m}}, \sigma_8)$ into $\Sigma_8 = \sigma_8(\Omega_{\mathrm{m}}/0.27)^{0.64}$ as done in F14. We plot the posterior of $\Sigma_8$ for the non-Gaussian data model in the bottom panel of Fig. 12 and obtain $\Sigma_8 = 0.79^{+0.08}_{-0.11}$ (grey area).

The constraining power of the non-Gaussian model for low values of $\sigma_8 \lesssim 0.7$, $\Omega_{\mathrm{m}} \lesssim 0.2$, and $\Sigma_8 \lesssim 0.7$ is slightly better compared to the Gaussian data model, as can be seen in the bottom panels of Figs 11 and 12 (compare the grey histogram to the blue dashed line). In addition to that, the black dotted lines show our non-Gaussian constraints for a fixed $h = 0.7$ without the marginalization of the Hubble parameter that all other results are subject to. The difference to the posterior in grey is small. Likewise, the impact of the 20 per cent error in the predicted model amplitude is also small, as indicated by the dotted–dashed green lines ($f = 0$).

The top panel of Fig. 12, displays the goodness of the SC01 model with respect to the CFHTLenS data. We plot the first five uncorrelated KL modes that are used in our analysis (red triangles). For comparison we also plot the KL modes of one random noisy clone data vector into the plot (open diamonds). The blue filled diamonds correspond to the best-fitting model of CFHTLenS with $\Omega_{\mathrm{m}} = 0.32$ and $\sigma_8 = 0.7$. We observe a clear discrepancy between the best fit and the CFHTLenS data at $n = 3$ and some weak discrepancy at $n = 2$. The $\chi^2$ of the residuals of the best fit is 4.2 per degree of freedom or $4.2/(1 + 20 \text{ per cent})^2 = 2.9$ if we account for a 20 per cent systematic error in the predicted amplitude; the systematic error can be included by increasing the errors of modes in the plot by 20 per cent. In order to illustrate that reasonable models are unable to fit the CFHTLenS data at $n = 3$, we have added the grey boxes to this figure. They depict the scatter of 68 per cent of the model amplitudes for parameters $\Sigma_8 \leq 1.0$ and
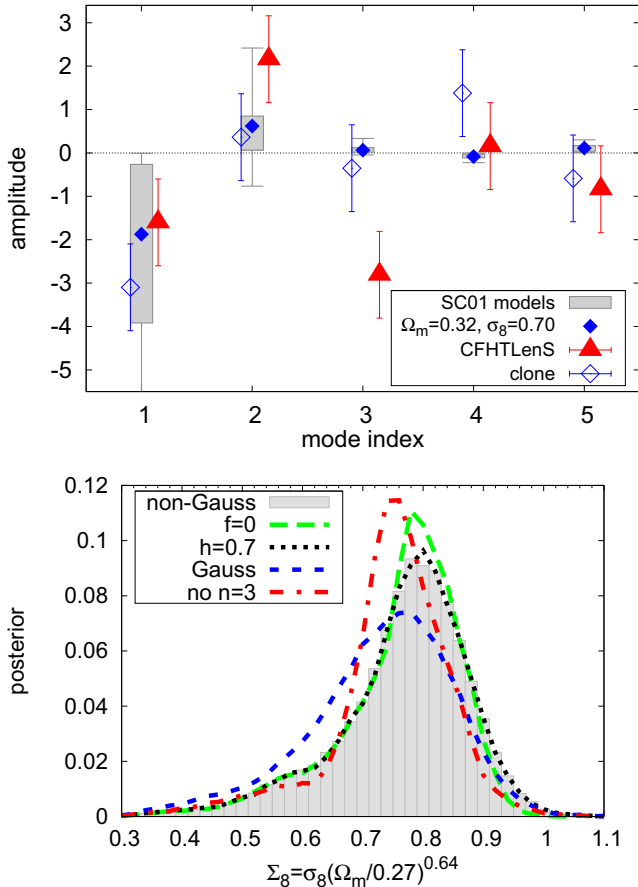
**Figure 12.** Top panel: the first five KL modes of the compressed CFHTLenS data vector (red triangles) in comparison to both the best-fitting model (filled blue diamonds) and the scatter of amplitudes of our models for a parameter range (grey whisker boxes). For the latter, the filled boxes denote the amplitude spread of 68 per cent of all models around the median for $\Sigma_8 = \sigma_8(\Omega_m/0.27)^{0.64} \leq 1.0$ and $h = 0.7$, whereas the whiskers bracket the entire amplitude range. There is a strong tension between models and data for $n = 3$. The error bars do not include the 20 per cent multiplicative error in the model amplitude. The $\chi^2$ per degree of freedom of CFHTLenS is 4.2 or 2.9 when the multiplicative error is included. The open diamonds denoted *clone* correspond to one random realization of a noisy clone measurement. Bottom panel: posterior of $\Sigma_8$ for the non-Gaussian data model (*non-Gauss*) for various strong priors (lines f = 0 and h = 0.7) compared to the posterior in the Gaussian model (line *Gauss*). The red dotted–dashed line shows the posterior based on the KL modes $n = 1, 2, 4, 5$ only.

$(\Omega_m, \sigma_8) \in [0.1, 1] \times [0.4, 1]$; current data constraints confine $\Sigma_8$ to about $0.76 \pm 0.06$ with 68 per cent confidence (F14). Additionally, the whiskers bracket the total amplitude range covered by the models. Clearly, our $n = 3$ mode is well outside the whisker region, underlining no model reproduces our measurement here. Note that mixed higher order moments between the errors of the KL modes may exist even though their second-order correlations vanish.

Finally, the red dotted–dashed line in the bottom panel of Fig. 12 corresponds to the posterior of $\Sigma_8$ leaving out the KL mode $n = 3$. Statistically the posterior is consistent with the constraint for *non-Gauss* although the mode of the distribution shifts to slightly smaller values of $\Sigma_8$ and tightens a bit, i.e. $\Sigma_8 = 0.77 \pm 0.08$.

## 7 DISCUSSION

We conclude from our results that the model of a Gaussian likelihood is sufficient for the cosmological analysis of the CFHTLenS $\langle M_{ap}^3 \rangle$ data, or data of comparable surveys, despite the evidence for a non-Gaussian distribution of errors. To arrive at this conclusion we measured the third moment $\langle M_{ap}^3 \rangle$ of the aperture mass for aperture scales between 5 and 30 arcmin. For this we excluded scales below 5 arcmin owing to indications of systematics in the aperture statistics. Our choice of 5 arcmin as smallest usable scale in the analysis had been made prior to the cosmological analysis of the data to avoid confirmation bias. Our maximum scale is determined by the geometry of the survey. For this angular range, the clone simulation of our data in Figs 7 and 8 indicates a moderate non-Gaussian distribution of the measurement errors between 10 and 30 arcmin. A Gaussian likelihood hence may produce biased parameter estimates in a cosmological analysis. To test the validity of a Gaussian likelihood, we performed a comparative cosmological analysis with a non-Gaussian likelihood that is constructed from the distribution of $\langle M_{ap}^3 \rangle$ estimates in our simulation. For this task, we devised a novel technique that involves a data compression to reduce the aperture statistics to a few essential uncorrelated modes that are shown in Fig. 12 (higher order correlations may be non-vanishing). Our statistical analysis factors in both measurement noise and uncertainties from the theory side without the need to specify the analytic form of the error PDF. This practical algorithm is an important contribution of this paper for future analyses because its applicability is not restricted to third-order shear statistics. The outcome of our statistical analysis for the two cosmological parameters $(\Omega_m, \sigma_8)$ is displayed in Fig. 11 and juxtaposed with a second analysis that uses a Gaussian likelihood. The posteriors of the parameters exhibit only little differences between the Gaussian and non-Gaussian likelihood – at least for a flat $\Lambda$CDM model which is strongly favoured by recent CMB constraints (Hinshaw et al. 2013; Planck Collaboration XVI 2014). The main difference between both models of the likelihood is illustrated by the bottom panels of Figs 11 and 12: the non-Gaussian model excludes more strongly low values of $\sigma_8$, the lower 68 per cent bound shifts up from 0.63 in the Gaussian case to 0.66 in the non-Gaussian; the lower limit of $\Sigma_8$ shifts from 0.60 to 0.68; the improvement of the lower limit of $\Omega_m$ is below 0.01. A qualitative similar behaviour for $\Omega_m$ and $\sigma_8$ was found with the non-Gaussian model of Hartlap et al. (2009) for the second-order statistics of cosmic shear. The observed changes are small compared to the width of the posteriors though. Consequently our results support the recent decision of F14 to apply a Gaussian model of the likelihood to angular scales smaller than 15 arcmin as reasonable approximation, although their cosmological constraints can probably be tightened by a non-Gaussian data model.

For future surveys with increased survey area and higher source number densities, we expect that non-Gaussian features will become more prominent in the data; a Gaussian model may hence then no longer be adequate. As seen in the top panels of Fig. 7, on small angular scales around 5 arcmin the signal is dominated by shape noise of the sources, which tends to Gaussianize the distribution of $\langle M_{ap}^3 \rangle$ for statistically independent intrinsic shapes. On larger scales of about 30 arcmin, on the other hand, cosmic variance is dominating, which on our subdegree scales is still non-Gaussian due to the non-linear clustering of matter (Fig. 8). For a fixed angular scale and for an increasingly higher number of source triplets in the estimator, the amplitude of cosmic variance grows greater relative to the shot noise variance. Hence future lensing surveys will exhibit stronger non-Gaussianities on the angular scales that are considered

here. However, for a quantitative assessment of the impact of these non-Gaussianities on parameter constraints with $\sim 10^3$ deg$^2$ surveys we need more independent simulated data vectors than the clone can provide. The clone allows only for about two independent realizations of a $\langle M_{ap}^3 \rangle$ measurement in this case. This is far too few to sample the data likelihood. Still, considering that we already see an inaccuracy with a Gaussian data model in CFHTLenS, we anticipate that a Gaussian model will potentially bias the cosmological analysis in future surveys.

Our posterior for $(\Omega_m, \sigma_8)$ from $\langle M_{ap}^3 \rangle$ only is highly degenerate, and it is 68 per cent consistent with recent constraints from the CMB and the Gaussian CFHTLenS analysis of F14. The degeneracy is shown in Fig. 11. The joint constraints on two parameters naturally have to be degenerate along a 1D line, as the cosmological information in the data essentially consists only of one significant KL mode, see Fig. 12. From the joint, degenerate constraints we infer $\Sigma_8 = \sigma_8 (\Omega_m/0.27)^{0.64} = 0.79^{+0.08}_{-0.11}$, in accordance with F14. Note that F14 used only cosmological scales between 5.5 and 15 arcmin as well as a more accurate model for the matter bispectrum which explains minor difference between our posterior contours. For a comparison to *WMAP*9 results, we break the parameter degeneracy by imposing a narrow prior on either parameter $\Omega_m$ or $\sigma_8$ that is consistent with *WMAP*9, i.e. $\Omega_m \in [0.25, 0.30]$ or $\sigma_8 \in [0.75, 0.85]$. For a prior on one parameter, the constraint of the other parameter is then also consistent with the *WMAP*9 best fit ($\sigma_8 = 0.82$ and $\Omega_m = 0.28$): we find $\Omega_m = 0.27^{+0.05}_{-0.05}$ and $\sigma_8 = 0.77^{+0.07}_{-0.11}$. The recent results from Planck Collaboration XVI (2014), on the other hand, favour somewhat larger best-fitting values $\sigma_8 = 0.83$ and $\Omega_m = 0.31$ due to a smaller $h = 0.67 \pm 0.014$. These values are also consistent with our CFHTLenS findings although there appears to be a $1\sigma$ tension between the values of $\Omega_m$. This tension is, however, comparable to the inaccuracy in our statistical methodology or model as seen in our verification run (bottom panel of Fig. 10); $\Omega_m$ and $\sigma_8$ are somewhat underestimated in the analysis. In conclusion, our $\langle M_{ap}^3 \rangle$ cannot distinguish a *WMAP*9 from a *Planck* cosmology; both are equally consistent with our CFHTLenS results.

In spite of the broad consistency of $(\Omega_m, \sigma_8)$ with the standard cosmology model, the CFHTLenS $\langle M_{ap}^3 \rangle$ data have features that cannot be explained by any of our SC01 models or more accurate models of the matter bispectrum in dark-matter-only universes (flat $\Lambda$CDM). A dark-matter-only model consequently is not good enough to describe our observed third-order correlations in the cosmic shear field, or there are remaining systematics in CFHTLenS on scales greater than $\sim 10$ arcmin that are relevant for the third-order statistics. The only moderately good model fit to the data becomes easily obvious when we inspect the compressed CFHTLenS data in Fig. 12; error bars are uncorrelated in this representation, and they have equal variance; the best fit has $\chi^2 = 4.2$ per degree of freedom without 20 per cent error in the model amplitude and $\chi^2 = 2.9$ including the amplitude error; the number of degrees of freedom is 3. All models with a generous cut of $\Sigma_8 \leq 1.0$ are essentially zero for KL modes $n \geq 3$. The CFHTLenS data at $n = 3$, on the other hand, is $3\sigma$ away from any of these models. Only models that are simultaneously large in $\Omega_m \sim 0.7$ and $\sigma_8 \sim 0.8$ get closer to the $n = 3$ data point but quickly move away from $n = 1$ and 5 at the same time and cannot explain our observation either; see e.g. the dashed–dotted line in the bottom panel of Fig. 9. The discrepancy is also visible in Fig. 6 where we plot the best-fitting model (filled squares) in comparison to the CFHTLenS data (open diamonds): the CFHTLenS data points are systematically above the model data points for $\theta_2 = 5.91$ arcmin (third column) in order to be consistent for larger values of $\theta_2$ (columns 4–5). Certainly, this disagreement

with theory, reflected by the $n = 3$ KL mode, could be a shortfall of SC01. However, no analytic model can be better than the bispectrum power in cosmological simulations that are used to either test or calibrate bispectrum models in the non-linear regime (SC01; Gil-Marin et al. 2012; Valageas et al. 2012). Therefore, improved modelling would at best reproduce the clone data points which are plotted in Fig. 9, open diamonds in the lower panel, and Fig. 12, filled triangles in the upper panel. Clearly, these data points do not exhibit the $n = 3$ feature seen in CFHTLenS; we find the same for the clone data points in the other 183 line-of-sights. Since both the clone and the CFHTLenS two-point statistics are consistent with the standard cosmological model (F14; Kitching et al. 2014), we therefore conclude that also a bispectrum model more advanced than SC01 or a dark-matter-only standard $\Lambda$CDM in general cannot explain our $n = 3$ mode of CFHTLenS. The $n = 3$ mode is most sensitive at $(\theta_1, \theta_2, \theta_3) = (5.9, 17.5, 30)$ and $(10.2, 17.5, 17.5)$ arcmin (top panel of Fig. 9). We hence broadly locate the discrepancy between $\theta \approx 10$ and 20 arcmin, or correspondingly $\ell \approx 248$ and 496.

Despite the evidence of some shear systematics in the data, we are unable to conclusively identify either IAs or residual PSF systematics as origin of the model discrepancy. However, there is evidence for IA playing only a minor role in this context. After the application of the systematics test in Appendix A, we additionally rejected nine CFHTLenS fields from the H12 sample. This mildly affects the third-order aperture statistics between 10 and 20 arcmin (left-hand panel of Fig. 4): the *pass fields* have a higher signal for the equilateral $\langle M_{ap}^3 \rangle$. We hence suspect that PSF systematics are at least in part responsible for a signal deficiency around 15 arcmin. Furthermore, after the removal of the early-type galaxies from our shear catalogue, we found little difference in the EEE signal but rather an increase of the BBB signal on small scales (Fig. 5). This behaviour is the opposite of what is expected for IA contaminated data: most of the IA signal is associated with early-type galaxies (Mandelbaum et al. 2006, 2011; Joachimi et al. 2011). Therefore it is unlikely that the signal drop near 15 arcmin as well as the remaining EEB, EBB, and BBB signals below 5 arcmin can be explained with IA. This supports theoretical models of IA that predict an insignificant contribution of IA correlations to the EEE signal above $\sim 5$ arcmin for CFHTLenS (Semboloni et al. 2008; Merkel & Schäfer 2014; Valageas 2014). In conclusion, further research is required to remove the remaining EEB, EBB, BBB systematics and to decide whether the tension between data and theoretical models persist. Finally, F14 do not report a significant B-mode on scales below 5 arcmin for the second-order aperture statistics. But they agree with our finding of an EEB, EBB, and BBB signal on these scales for the third-order statistics. This suggests that the here reported PSF systematics become only relevant for higher order cosmic shear statistics.

As additional online material we provide a Monte Carlo sample of $(\Omega_m, \sigma_8)$ based on the posterior in the top left-hand panel of Fig. 11 and a set of 200 realizations of $\langle M_{ap}^3 \rangle$ data vectors that we produced from our *noisy* clone simulations.

## ACKNOWLEDGEMENTS

## REFERENCES

Asgari M., Schneider P., 2014, preprint (arXiv:1409.0863)
Bartelmann M., Schneider P., 2001, Phys. Rep., 340, 291
Benitez N., 2000, ApJ, 536, 571
Benjamin J. et al., 2007, MNRAS, 381, 702
Benjamin J. et al., 2013, MNRAS, 431, 1547
Bergé J., Amara A., Réfrégier A., 2010, ApJ, 712, 992
Bernardeau F., van Waerbeke L., Mellier Y., 1997, A&A, 322, 1
Bernardeau F., van Waerbeke L., Mellier Y., 2003, A&A, 397, 405
Calabretta M., Greisen E. W., 2000, in Manset N., Veillet C., Crabtree D., eds, ASP Conf. Ser. Vol. 216, Astronomical Data Analysis Software and Systems IX. Astron. Soc. Pac., San Francisco, p. 571
Cooray A., Hu W., 2002, ApJ, 574, 19
Crittenden R. G., Natarajan P., Pen U.-L., Theuns T., 2002, ApJ, 568, 20
de Jong J. T. A. et al., 2013, The Messenger, 154, 44
Dodelson S., 2003, Modern Cosmology. Academic Press, Amsterdam
Eifler T., Schneider P., Hartlap J., 2009, A&A, 502, 721
Eisenstein D. J., Hu W., 1998, ApJ, 496, 605
Erben T. et al., 2013, MNRAS, 433, 2545
Fu L. et al., 2008, A&A, 479, 9
Fu L. et al., 2014, MNRAS, 441, 2725 (F14)
Gillis B. R. et al., 2013, MNRAS, 431, 1439
Gil-Marin H., Wagner C., Fragkoudi F., Jimenez R., Verde L., 2012, J. Cosmol. Astropart. Phys., 2, 47
Hamana T., Colombi S. T., Thion A., Devriendt J. E. G. T., Mellier Y., Bernardeau F., 2002, MNRAS, 330, 365
Hamilton A. J. S., Rimes C. D., Scoccimarro R., 2006, MNRAS, 371, 1188
Harnois-Déraps J., van Waerbeke L., 2014, MNRAS, submitted (arXiv:1406.0543)
Harnois-Déraps J., Vafaei S., van Waerbeke L., 2012, MNRAS, 426, 1262
Harnois-Déraps J., van Waerbeke L., Viola M., Heymans C., 2014, preprint (arXiv:1407.4301)
Hartlap J., Simon P., Schneider P., 2007, A&A, 464, 399
Hartlap J., Schrabback T., Simon P., Schneider P., 2009, A&A, 504, 689
Heavens A., Refregier A., Heymans C., 2000, MNRAS, 319, 649
Heitmann K., Lawrence E., Kwan J., Habib S., Higdon D., 2014, ApJ, 780, 111
Heymans C. et al., 2012, MNRAS, 427, 146 (H12)
Heymans C. et al., 2013, MNRAS, 432, 2433
Hildebrandt H. et al., 2012, MNRAS, 421, 2355
Hinshaw G. et al., 2013, ApJS, 208, 19
Hirata C. M., Seljak U., 2003, Phys. Rev. D, 68, 083002
Hoekstra H. et al., 2006, ApJ, 647, 116
Hyvarinen A., 1999, IEEE Trans. Neural Networks, 10, 626
Jarvis M., Bernstein G., Jain B., 2004, MNRAS, 352, 338
Joachimi B., Mandelbaum R., Abdalla F. B., Bridle S. L., 2011, A&A, 527, A26
Kayo I., Takada M., Jain B., 2013, MNRAS, 429, 344
Keitel D., Schneider P., 2011, A&A, 534, A76
Kilbinger M., 2014, Rep. Progress Phys., submitted (arXiv:1411.0115)
Kilbinger M., Munshi D., 2006, MNRAS, 366, 983
Kilbinger M., Schneider P., 2005, A&A, 442, 69
Kilbinger M. et al., 2013, MNRAS, 430, 2200
Kitching T. D., Miller L., Heymans C. E., van Waerbeke L., Heavens A. F., 2008, MNRAS, 390, 149
Kitching T. D. et al., 2012, MNRAS, 423, 3163
Kitching T. D. et al., 2014, MNRAS, 442, 1326
Komatsu E. et al., 2009, ApJS, 180, 330
Laureijs R. et al., 2011, preprint (arXiv:1110.3193)
Li Y., Hu W., Takada M., 2014, Phys. Rev. D, 89, 083519
Loftsgaarden D., Quesenberry C., 1965, Ann. Math. Stat., 36, 1049
LSST Science Collaboration et al., 2009, priprint (arXiv:0912.0201)
Mandelbaum R., Hirata C. M., Ishak M., Seljak U., Brinkmann J., 2006, MNRAS, 367, 611
Mandelbaum R. et al., 2011, MNRAS, 410, 844
Merkel P. M., Schäfer B. M., 2014, MNRAS, 445, 2918
Miller L., Kitching T. D., Heymans C., Heavens A. F., van Waerbeke L., 2007, MNRAS, 382, 315
Miller L. et al., 2013, MNRAS, 429, 2858
Miyazaki S. et al., 2012, Proc. SPIE Vol. 8446, Society of Photo-Optical Instrumentation Engineers (SPIE) Conf. Series

Pen U.-L., Zhang T., van Waerbeke L., Mellier Y., Zhang P., Dubinski J., 2003, ApJ, 592, 664

Planck Collaboration XVI, 2014, A&A, 571, A16

Press W. H., Teukolsky S. A., Vetterling W. T., Flannery B. P., 1992, Numerical Recipes in C: The Art of Scientific Computing, 2nd edn. Cambridge Univ. Press, New York

Rimes C. D., Hamilton A. J. S., 2006, MNRAS, 371, 1205

Sato M., Ichiki K., Takeuchi T. T., 2011, Phys. Rev. D, 83, 023501

Schneider P., 2003, A&A, 408, 829

Schneider P., 2006, in Meylan G., Jetzer P., North P., Schneider P., Kochanek C. S., Wambsganss J., eds, Saas-Fee Advanced Course 33, Gravitational Lensing: Strong, Weak and Micro. Springer-Verlag, Berlin, p. 269

Schneider P., Lombardi M., 2003, A&A, 397, 809

Schneider P., van Waerbeke L., Jain B., Kruse G., 1998, MNRAS, 296, 873

Schneider P., Kilbinger M., Lombardi M., 2005, A&A, 431, 9

Schneider P., Eifler T., Krause E., 2010, A&A, 520, A116

Scoccimarro R., Couchman H. M. P., 2001, MNRAS, 325, 1312 (SC01)

Semboloni E. et al., 2006, A&A, 452, 51

Semboloni E., Heymans C., van Waerbeke L., Schneider P., 2008, MNRAS, 388, 991

Semboloni E., Schrabback T., van Waerbeke L., Vafaei S., Hartlap J., Hilbert S., 2011, MNRAS, 410, 143

Semboloni E., Hoekstra H., Schaye J., van Daalen M. P., McCarthy I. G., 2011, MNRAS, 417, 2020

Simon P. et al., 2013, MNRAS, 430, 2476

Simpson F. et al., 2013, MNRAS, 429, 2249

Smith R. E. et al., 2003, MNRAS, 341, 1311

Takada M., Jain B., 2003, MNRAS, 344, 857

Takahashi R., Sato M., Nishimichi T., Taruya A., Oguri M., 2012, ApJ, 761, 152

Taylor A., Joachimi B., Kitching T., 2013, MNRAS, 432, 1928

Tegmark M., Taylor A. N., Heavens A. F., 1997, ApJ, 480, 22

The Dark Energy Survey Collaboration, 2005, preprint (arXiv:astro-ph/0510346)

Vafaei S., Lu T., van Waerbeke L., Semboloni E., Heymans C., Pen U.-L., 2010, Astropart. Phys., 32, 340

Valageas P., 2014, A&A, 561, A53

Valageas P., Nishimichi T., 2011a, A&A, 527, A87

Valageas P., Nishimichi T., 2011b, A&A, 532, A4

Valageas P., Sato M., Nishimichi T., 2012, A&A, 541, A162

van Waerbeke L., 1998, A&A, 334, 1

van Waerbeke L., Bernardeau F., Mellier Y., 1999, A&A, 342, 15

van Waerbeke L., Hamana T., Scoccimarro R., Colombi S., Bernardeau F., 2001, MNRAS, 322, 918

van Waerbeke L. et al., 2013, MNRAS, 433, 3373

Velander M. et al., 2014, MNRAS, 437, 2111

Wilking P., Schneider P., 2013, A&A, 556, A70

Zhang L. L., Pen U.-L., 2005, New Astron., 10, 569

## APPENDIX A: REFINED TEST FOR SHEAR SYSTEMATICS

The level of residual systematics in the CFHTLenS lensing catalogue is quantified by H12 using the two-point shear statistics. It is therefore not guaranteed that residual systematics for higher order statistics would lead to the same field selection. For this paper, we therefore assess the level of systematics affecting three-point shear statistics by using a refinement of the H12 methodology. We apply the refined test to the 129 CFHTLenS pointings that have already passed the systematics criteria of H12. Out of these 129 we reject another nine pointings for our cosmological analysis of the three-point shear statistics. The details of the refinement and its results for CFHTLenS follow below.

### A1 Description of the method

We adopt the residual systematics PSF model of H12: any residual systematics is a linear combination of the stellar anisotropy $\epsilon_a^\star$ of all exposures $a$. Therefore, the observed galaxy ellipticity, $\epsilon^{\mathrm{obs}}$, originating from the lack of a perfect PSF correction, is given by

$$\epsilon_i^{\mathrm{obs}} = \epsilon_i^{\mathrm{int}} + \gamma_i + \eta_i + \sum_{a=1}^{n_{\mathrm{exp}}} \alpha_a \epsilon_{a,i}^\star, \quad i = 1, 2. \tag{A1}$$

This thus expresses, for each ellipticity component $i$, the observed (PSF-corrected) ellipticity $\epsilon_i^{\mathrm{obs}}$ as sum of (i) the intrinsic ellipticity $\epsilon_i^{\mathrm{int}}$, (ii) the cosmic shear $\gamma_i$, and (iii) the random noise $\eta_i$. In addition, (iv) the last term expresses the PSF residual systematic error at the location of the galaxy as a linear combination of the original PSF ellipticity $\epsilon_a^\star$ directly measured from the stars in each exposure $a$ out of $n_{\mathrm{exp}}$ exposures; the $\alpha_a$ are the coefficients of the linear combination.

Moreover, following the conclusion from H12 we assume that the zero-lag correlations of the ellipticities already contain all the relevant information about the residual PSF correlations for the three-point correlation functions. For the PSF residuals described by equation (A1), the average measured zero-lag on a given pointing is

$$\langle \epsilon_i^{\mathrm{obs}} \epsilon_j^{\mathrm{obs}} \epsilon_k^{\mathrm{obs}} \rangle = \langle \gamma_i \gamma_j \gamma_k \rangle + \langle \Delta(\epsilon_i^{\mathrm{obs}} \epsilon_j^{\mathrm{obs}} \epsilon_k^{\mathrm{obs}}) \rangle, \tag{A2}$$

where $i, j, k = 1, 2$ indicate the projections of $\epsilon^{\mathrm{obs}}$ and $\gamma$, and

$$\langle \Delta(\epsilon_i^{\mathrm{obs}} \epsilon_j^{\mathrm{obs}} \epsilon_k^{\mathrm{obs}}) \rangle$$
$$= \sum_{a,b,c=1}^{n_{\mathrm{exp}}} \alpha_a \alpha_b \alpha_c \langle \epsilon_{a,i}^\star \epsilon_{b,j}^\star \epsilon_{c,k}^\star \rangle$$
$$+ 3 \left[ \langle \gamma_j \gamma_k \rangle + \langle \eta_j \eta_k \rangle + \langle \epsilon_j^{\mathrm{int}} \epsilon_k^{\mathrm{int}} \rangle \right] \sum_{a=1}^{n_{\mathrm{exp}}} \alpha_a \langle \epsilon_{a,i}^\star \rangle. \tag{A3}$$

The indices $(a, b, c)$ indicate the various exposures, while the average $\langle \cdots \rangle$ is over all zero-lag triplets. Similarly, the PSF–galaxy cross-correlations are

$$\langle \epsilon_i^{\mathrm{obs}} \epsilon_j^{\mathrm{obs}} \epsilon_{a,k}^\star \rangle$$
$$= \left[ \langle \gamma_i \gamma_j \rangle + \langle \eta_i \eta_j \rangle + \langle \epsilon^{\mathrm{int}} \epsilon^{\mathrm{int}} \rangle \right] \langle \epsilon_{a,k}^\star \rangle$$
$$+ \sum_{b,c=1}^{n_{\mathrm{exp}}} \alpha_a \alpha_b \alpha_c \langle \epsilon_{a,k}^\star \epsilon_{b,i}^\star \epsilon_{c,j}^\star \rangle \tag{A4}$$

and

$$\langle \epsilon_i^{\mathrm{obs}} \epsilon_{a,j}^\star \epsilon_{b,k}^\star \rangle = \sum_{c=1}^{n_{\mathrm{exp}}} \alpha_c \langle \epsilon_{c,i}^\star \epsilon_{a,j}^\star \epsilon_{b,k}^\star \rangle. \tag{A5}$$

We estimate the zero-lag triplets by interpolating the stellar anisotropy at the position of the source galaxy. For the derivation of the equations (A3)–(A5), we assume that the PSF is uncorrelated with the intrinsic ellipticity, the shear, and the random noise. In the absence of any systematics, equations (A3)–(A5) have to vanish, hence a non-zero signal for either average can be used as indicator for systematics. However, in the presence of systematics the expectation values of both (A3) and (A4) do directly depend on cosmology through the terms $\langle \gamma_i \gamma_j \gamma_k \rangle$ and $\langle \gamma_i \gamma_j \rangle$, and they depend on the details of IA through $\langle \epsilon_j^{\mathrm{int}} \epsilon_k^{\mathrm{int}} \rangle$. Therefore, for an evaluation of the significance of a non-zero signal we have to assume a fiducial model for the shear and IA correlations. Conversely, the expectation value of (A5) is free of these assumption so that we focus on (A5) as

systematics indicator in the following. Nevertheless some cosmology dependence enters for this indicator too because the variance of this indicator,

$$
\left\langle \left( \epsilon_i^{\mathrm{obs}} \epsilon_{a,j}^* \epsilon_{b,k}^* \right)^2 \right\rangle = \left\langle \left( \epsilon_i^{\mathrm{int}} + \gamma_i + \eta_i \right)^2 \right\rangle \left\langle \left( \epsilon_{a,j}^* \epsilon_{b,k}^* \right)^2 \right\rangle
$$
$$
+ \left\langle \left( \sum_{c=1}^{n_{\mathrm{exp}}} \alpha_c \epsilon_{c,i}^* \epsilon_{a,j}^* \epsilon_{b,k}^* \right)^2 \right\rangle, \tag{A6}
$$

contains second-order correlations between $\gamma_i$ and $\epsilon_j^{\mathrm{int}}$ on the right-hand side; the intrinsic variance for the null hypothesis, i.e. no systematics, has to be known to test for a presence of systematics. Contrary to (A3) and (A4) however, we expect a weak impact of the cosmology on the test results, though, as on small scales (zero-lag) the variance $\langle (\epsilon_i^{\mathrm{int}} + \gamma_i + \eta_i)^2 \rangle \approx \langle (\epsilon_i^{\mathrm{int}})^2 \rangle$ is likely dominated by shape noise.

### A2  Null hypothesis

In the following, we describe the set of simulations we use for the measurement of the PDF of the systematics indicator $\langle \epsilon_i^{\mathrm{obs}} \epsilon_{a,j}^* \epsilon_{a,k}^* \rangle$ for the null hypothesis. This distribution is the key element in the evaluation of the residual systematics for the three-points function measurement. Using the same set of simulations described in H12, there are 160 realizations per pointing available, each with a shear signal assigned from a projected mass map extracted from independent lines-of-sights. These maps originate from the same *N*-body simulations that have been used for the clone. This means for the null hypothesis

(i) a *WMAP*5 cosmology;
(ii) no IAs of the sources;
(iii) no correlations of intrinsic ellipticities and shear;
(iv) no B-modes of the shear field;
(v) distribution of intrinsic shapes and source positions as in CFHTLenS.

A shear value is assigned to each galaxy, depending on its 3D position in the sky. Shape noise is added to the shear as an ellipticity component obtained by randomizing the orientation of the ellipticity of the CFHTLenS galaxies. This procedure guarantees that the simulated catalogues have similar shape noise and intrinsic ellipticity characteristics as the real CFHTLenS pointing. Note that the simulated shape noise is marginally larger than in the real data because the shear is also randomized when computing the noise, it is not removed; this is only a 1 per cent effect and hence negligible for the test. For each pointing, we create 1600 realizations by generating for each of the 160 lines-of-sight 10 different noise realizations. The PSF ellipticity at each galaxy location, $\epsilon_a^\star$ is derived from the LENSFIT PSF model (Miller et al. 2013). For each pointing, the PDF of $\langle \epsilon_i^{\mathrm{obs}} \epsilon_{a,j}^\star \epsilon_{a,k}^\star \rangle$ is then constructed from the distribution of (A5) in the 1600 realizations.

The probability of measuring a given value of

$$
\Xi_i = \sum_{a=1}^{n_{\mathrm{exp}}} \left\langle \epsilon_i^{\mathrm{obs}} \epsilon_{a,i}^\star \epsilon_{a,i}^\star \right\rangle, \quad i = 1, 2 \tag{A7}
$$

for a CFHTLenS pointing given its specific PSF and noise properties can now be quantified against the assumptions of the null hypothesis. We obtain the zero-lag correlation $\langle \epsilon_i^{\mathrm{obs}} \epsilon_{a,j}^\star \epsilon_{b,k}^\star \rangle$ by interpolating $\epsilon_{a,j}^\star$ and $\epsilon_{a,k}^\star$ at the position of the galaxy with $\epsilon^{\mathrm{obs}}$. For simplicity, we restrict the analysis to the correlations $\langle \epsilon_i^{\mathrm{obs}} \epsilon_{a,i}^\star \epsilon_{a,i}^\star \rangle$ measured in the same exposure *a*, and then sum over all the exposures of a given pointing; cross-correlations between exposures are
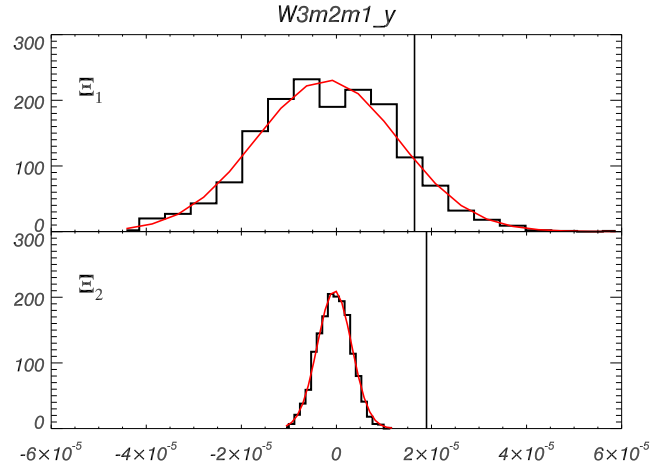


**Figure A1.** Top panel: comparison of the systematics indicators $\Xi_i$ of W3m2m1_y (vertical black line) to the simulated distribution of the null hypothesis (histogram). The red solid line is the best-fitting Gaussian to the histogram. The $\Xi_1$ is consistent with no systematics. Bottom panel: the same as the top panel but for $\Xi_2$. Here the measured value is inconsistent with the null hypothesis on a high confidence level; the pointing is hence rejected for the cosmological analysis of $\langle M_{\mathrm{ap}}^3 \rangle$.

ignored. This strategy provides the strongest signal. We then judge the systematics significance of a value of $\Xi_i$ in CFHTLenS by the correlation excess with respect to our simulated PDF. See Fig. A1, based on the pointing W3m2m1_y, as an example. Here we plot the null hypothesis as histogram (black solid lines) that we successfully fit by a Gaussian distribution (red solid lines). The vertical solid lines are the corresponding actual values in CFHTLenS for comparison. We reject this pointing due to its large excess of $\Xi_2$.

### A3  Application to the CFHTLenS data

We evaluate the cross-correlation defined in (A5) for each pair of exposures $(a, b)$ and for different projections $(i, j, k)$ of the vectors $(\epsilon^\star, \epsilon^{\mathrm{obs}})$. From this, we estimate the statistics $\Xi_i$ for every CFHTLenS pointing and test the values against the null hypothesis. For this test, we assume that a Gaussian distribution is a good approximation of the null distribution of $\Xi_i$. This is a valid assumption for the two-point cross-correlations (see H12), and we have checked that it is also a valid assumption for histograms of $\Xi_i$, which we fit by a Gaussian of mean $\nu_i$ and variance $\sigma_i$ for every pointing. As expected, the averages $\nu_i$ are always consistent with zero.

As a null $\Xi_i$ is supposed to obey Gaussian statistics, 31.80 per cent of the pointings should have $|\Xi_i| > \sigma_i$, 4.6 per cent should have $|\Xi_i| > 2\sigma_i$, and 0.04 per cent should have $|\Xi_i| > 3\sigma_i$. Table A1

**Table A1.** Number of pointings with $|\Xi_i|$ below $\sigma_i$ (first line), $2\sigma_i$ (second line), and $3\sigma_i$ (third line); $\sigma_i$ is the standard deviation of the null hypothesis (no systematics). We indicate in parentheses the fractional value corresponding to this number. We show the results both for $\Xi_1$ (first column) and $\Xi_2$ (second column) as well as the expectation for a null signal (third column). The total number of 129 pointings used here complies with the systematics criteria of H12.

|  | $\Xi_1$ | $\Xi_2$ | Null (Gaussian) |
|---|---|---|---|
| $|\Xi_i| < \sigma_i$ | 90 (70 per cent) | 69 (53 per cent) | ∼80 (68.2 per cent) |
| $|\Xi_i| < 2\sigma_i$ | 126 (98 per cent) | 109 (84 per cent) | ∼123 (95.4 per cent) |
| $|\Xi_i| < 3\sigma_i$ | 129 (100 per cent) | 124 (96 per cent) | ∼129 (99.6 per cent) |

compares systematics indicators of 129 CFHTLenS pointings to the null hypothesis with respect to the $\sigma_i$, $2\sigma_i$, and $3\sigma_i$ thresholds. These 129 pointings have been pre-selected by the criteria defined in H12. Within $3\sigma_i$ the statistics of $|\Xi_1|$ is consistent with the null hypothesis, whereas $|\Xi_2|$ reveals too many outliers with $|\Xi_2| > 3\sigma_i$.

For the final cosmological analysis, we decided to reject pointings that are within the Gaussian 1 per cent tail of the null hypothesis. The false-positive rate of our test is consequently 1 per cent. Based on this cut, we reject the following pointings: W1m3p3_i, W1p3p1_y, W2m1m0_i, W3m3m0_i, W3m2m1_y, W3p1m1_i, W4m3p1_i, W4m3m0_i, and W4m3p3_y. All these fields are rejected owing to too high values of $|\Xi_2|$ alone. The signal with and without the rejected fields can be seen in the left-hand panel of Fig. 4.

## SUPPORTING INFORMATION

Additional Supporting Information may be found in the online version of this article:

**Simon-etal2014-onlinematerial.tar.gz**

([http://mnras.oxfordjournals.org/lookup/suppl/doi:10.1093/mnras/stv339/-/DC1](http://mnras.oxfordjournals.org/lookup/suppl/doi:10.1093/mnras/stv339/-/DC1)).

Please note: Oxford University Press are not responsible for the content or functionality of any supporting materials supplied by the authors. Any queries (other than missing material) should be directed to the corresponding author for the article.

This paper has been typeset from a TEX/LATEX file prepared by the author.